



1 **Satellite-based Near-Real-Time Global Daily Terrestrial** 2 **Evapotranspiration Estimates**

3 Lei Huang^{1*}, Yong Luo^{1*}, Jing M. Chen^{2,3}, Qihong Tang^{4,5}, Tammo Steenhuis⁶, Wei
4 Cheng⁷ and Wen Shi¹

5 ¹Department of Earth System Science, Ministry of Education Key Laboratory for Earth System Modeling,
6 Institute for Global Change Studies, Tsinghua University, Beijing 100084, China

7 ²Key Laboratory for Humid Subtropical Ecogeographical Processes of the Ministry of Education, School
8 of Geographical Sciences, Fujian Normal University, Fuzhou, 350007, China

9 ³Department of Geography and Planning, University of Toronto, Ontario, M5S 3G3, ON, Canada

10 ⁴Key Laboratory of Water Cycle and Related Land Surface Processes, Institute of Geographic Sciences
11 and Natural Resources Research, Chinese Academy of Sciences, Beijing 100101, China

12 ⁵University of Chinese Academy of Sciences, Beijing 101408, China

13 ⁶Department of Biological and Environmental Engineering, Cornell University, Ithaca 14850, New York,
14 USA

15 ⁷Key Laboratory of Land Surface Pattern and Simulation, Institute of Geographic Sciences and Natural
16 Resources Research, Chinese Academy of Sciences, Beijing 100101, China

17

18 *Correspondence to* Lei Huang (leihuang007@mail.tsinghua.edu.cn) or
19 Yong Luo (Yongluo@mail.tsinghua.edu.cn)

20

21 **Abstract.**

22 Accurate and timely information on global terrestrial actual evapotranspiration (ET) is crucial in
23 agriculture, water resource management and drought forecasting in a changing climate. While numerous
24 satellite-based ET products have been developed in recent decades, few provide near-real-time global
25 terrestrial ET estimates. The MOD16 ET dataset, currently updating at the fastest rate, still experiences
26 a delay of over two weeks. This is because most satellite-based ET algorithms rely on meteorological
27 data from land surface models or in situ measurements, which cannot be obtained in near-real-time,
28 resulting in delays of more than two weeks. To expedite global ET data access, we developed the
29 Moderate Resolution Imaging Spectroradiometer (MODIS) based Variation of Standard
30 Evapotranspiration Algorithm (VISEA) to provide global daily ET data within a week of the actual
31 measurements at a spatial resolution of 0.05°. The VISEA model incorporates several key components:
32 (1) A vegetation index (VI)-temperature (Ts) triangle method to simulate air temperature (Ta), serves as
33 a basis for calculating other meteorological parameters (e.g., water vapor deficit and wind speed); (2) A
34 daily evaporation fraction (EF) method based on the decoupling parameter, converts satellite-based
35 instantaneous observations into daily ET estimates; (3) A net radiation calculation program takes into
36 account cloud coverage in the atmosphere's downward longwave radiation. The VISEA model is driven
37 by shortwave radiation from the European Centre for Medium-range Weather Forecasts (ERA5-Land)
38 and MODIS land products, e.g., surface reflectance, land surface temperature/emissivity, land cover
39 products), vegetation indices, and albedo as inputs. To assess its accuracy, we compared VISEA-with
40 measurements from 149 flux towers, five other satellite-based global ET products, and precipitation data
41 from the Global Precipitation Climatology Centre (GPCP). The evaluations show that the near-real-time
42 ET using VISEA performs with similar accuracy to other existing data products and offers a significantly
43 shorter time frame for daily data availability. Over 12 landcover types, the mean R is about 0.6 with an
44 RMSE of 1.4 mm day⁻¹ at a daily scale. Furthermore, the consistent spatial patterns of multi-year average



45 VISEA align closely with GPCP precipitation data, reaffirming the dataset's ability to accurately
46 represent global terrestrial ET distribution. To emphasize the capabilities of the VISEA for drought
47 monitoring, we analyzed the spatial and temporal variations of ET during a drought event and subsequent
48 recovery with precipitation in the Yangtze River basin from August 28th to September 1st, 2022. The
49 VISEA distinctly illustrated low ET levels ($<0.2 \text{ mm day}^{-1}$) across most areas of the Yangtze River Basin
50 on August 28th, indicating the severity of the drought. Conversely, a noticeable increase in ET ($>0.9 \text{ mm}$
51 day^{-1}) is observed on August 29th, signifying the retreat of the drought due to precipitation. The near-real-
52 time global daily terrestrial ET estimates could be valuable for meteorology and hydrology applications
53 requiring real-time data, particularly in coordinating relief efforts during droughts. The VISEA code and
54 dataset are available at <https://doi.org/10.11888/Terre.tpd.300782> (Huang et al., 2023a).

55 **1 Introduction**

56 Global terrestrial evapotranspiration (ET) is a vital component of the Earth's water cycle and energy
57 budget. It includes evaporation from the soil and water surfaces (some studies also consider evaporation
58 from the intercepted precipitation in canopies) and plant transpiration (Zhang et al., 2021; He et al., 2022).
59 Accurate and timely estimation of ET is essential for quantitatively assessing changes in the water cycle
60 under climate change, vigilant monitoring drought, and effectively managing and allocating water
61 resources (Su et al., 2020; Han et al., 2021; Aschonitis et al., 2022).

62 While near-real-time ET estimation from climate models is widely used to assess and predict ET
63 changes in the global water cycle under different weather conditions (Copernicus Climate Change
64 Service, 2020), these models often have limited spatial resolutions, making them less effective for
65 assessing drought conditions and optimizing water allocation. On the other hand, obtaining highly
66 accurate, near-real-time, or real-time ET measurements through local eddy covariance or lysimeter
67 methods can be very valuable (Awada et al., 2022), but collecting large-scale ET data using this
68 equipment proves to be quite challenging (Barrios et al., 2015; Tang et al., 2009).

69 Remote sensing presents a promising method for near-real-time estimation of global terrestrial ET
70 by offering timely observed land surface data. Several satellite-based ET datasets have emerged in recent
71 decades, each utilizing different algorithms such as the Penman-Monteith-based ET products like MODIS
72 ET (MOD16), developed by Mu et al. (2007, 2011), the Advanced Very High Resolution Radiometer
73 (AVHRR) ET by Zhang et al. (2006, 2009), and the Penman-Monteith-Leuning Evapotranspiration V2
74 (PML_V2, or simply PML) developed by Zhang et al. (2019, 2022). In addition, the Global Bio-
75 Atmosphere Flux (GBAF, also known as FluxCom) uses a machine learning approach with data from
76 flux towers, meteorology, and hydrology, published by Jung et al. (2009, 2010, 2019). Finally, the
77 Priestley-Taylor equation-based Global Land Evaporation Amsterdam Model (GLEAM) ET was
78 developed by Miralles et al. (2011b) and Martens et al. (2017). While these satellite-based global ET
79 products yield reasonable estimations, they cannot provide near-real-time ET estimates. Despite the
80 ongoing rapid updates of the MOD16 ET dataset, it still encounters a delay exceeding two weeks.
81 Additionally, AVHRR ET spans from 1983 to 2006, PML ET covers the period from 2002 to 2019,
82 GBAF covers from 2001 to 2015, and GLEAM ET extends from 2003 to 2020. Notably, the four later



83 ET products exhibit data gaps exceeding one year, posing challenges for near-real-time estimation.
84 Additionally, NASA's ECOSystem Spaceborne Thermal Radiometer Experiment on Space Station
85 (ECOSTRESS) intends to deliver global-scale ET estimation (Fisher et al., 2020). Unfortunately, as of
86 now, the data from ECOSTRESS have not been published. This data gap means there is still a lack of
87 satellite-based global near-real-time ET estimation.

88 The Variation of the Moderate Resolution Imaging Spectroradiometer Standard Evapotranspiration
89 Algorithm (VISEA) was introduced by Tang et al. (2009), which was designed for the near-real-time
90 monitoring of crop consumption at the basin scale. Huang et al. (2017) examined its reliability by
91 conducting a comprehensive assessment comparing its ET values with flux tower measurements and
92 other gridded ET datasets across various scales in China. Subsequently, to improve the model, a
93 decoupling parameter for daily evaporation fraction (EF) was introduced (Huang et al., 2021), and the
94 atmospheric emissivity and cloud coverage in the daily net radiation calculation was included (Huang et
95 al., 2023b). Global terrestrial application and evaluation of the developed VISEA algorithm have not
96 been conducted so far. In this study, we employ this VISEA algorithm along with MODIS surface
97 reflectance (MOD09CMG) (Vermote, 2015), land surface temperature/emissivity (MOD11C1) (Wan et
98 al., 2015), land cover products (MCD12C1) (Friedl & Sulla-Menashe, 2015), vegetation indices
99 (MOD13C1) (Didan, 2015), albedo (MCD43C3) (Schaaf & Wang 2015), and hourly shortwave radiation
100 from ECMWF ERA5-Land (Sabater, 2019) to provide global daily ET estimates from 2001 to 2022.

101 The performance of VISEA was evaluated with data from meteorological instruments and eddy
102 covariance measurements at 149 flux towers of FLUXNET (Pastorello et al., 2020). We assessed the
103 spatial distribution averages of VISEA by comparing its multi-year average with established ET datasets
104 GLEAM (Martens et al., 2017; Miralles et al., 2011), GBAF (Jung et al., 2009, 2010, 2018), AVHRR
105 (Zhang et al., 2009, 2010), MOD16 (Mu et al., 2007, 2011), PML (Zhang et al., 2019, 2022) and
106 precipitation data from the Global Precipitation Climatology Centre (GPCC) (Udo et al., 2011).

107

108 2. Methods

109 2.1 Description of the VISEA algorithm

110 VISEA, short for the Variation of the Moderate Resolution Imaging Spectroradiometer Standard
111 Evapotranspiration Algorithm, is a modification of the MODIS standard Evapotranspiration (ET)
112 algorithm. The original MODIS algorithm, created by Mu et al. (2007 and 2011), is based on the Penman-
113 Monteith method. VISEA introduces two significant modifications. First, it employs the Vegetation (VI)-
114 Temperature (Ts) Triangle method, originally developed by Nishida et al. (2003), to estimate air
115 temperature. Second, VISEA incorporates hourly data on shortwave downward radiation from the ERA5-
116 Land dataset to calculate daily average energy. These two advancements enable VISEA to estimate large-
117 scale ET without needing local measurements as supplementary data.

118 Unlike energy budget-based ET algorithms (such as SEBS, METRIC, and Alexi) that rely on
119 the direct use of thermal information, VISEA estimates ET using the Penman-Monteith equation, placing



120 it in a different category of satellite-based global ET products currently in use. VISEA is a two-source
121 model, which means the ET in one grid cell was separated as the transpiration from full vegetation cover
122 and the evaporation from bare soil surface if energy transfer from the vegetation to the soil surface was
123 ignored (Nishida et al., 2003), i.e.,

$$124 \quad ET = f_{veg}ET_{veg} + (1 - f_{veg})ET_{soil} \quad (1)$$

125 where the subscript " veg " means full vegetation cover and the subscript "soil" indicates the soil exposed
126 to solar radiation (called bare soil); ET_{veg} is the transpiration from full vegetation cover area ($W m^{-2}$),
127 ET_{soil} is the evaporation from bare soil ($W m^{-2}$), f_{veg} is the portion of the area with the vegetation cover,
128 which can be calculated by Normalized Difference Vegetation Index, $NDVI$ (Tang et al., 2009):

$$129 \quad f_{veg} = \frac{NDVI - NDVI_{min}}{NDVI_{max} - NDVI_{min}} \quad (2)$$

130 where the $NDVI$ is the Normalized Difference Vegetation Index and can be calculated as:

$$131 \quad NDVI = \frac{R_{nir} - R_{red}}{R_{nir} + R_{red}} \quad (3)$$

132 where $NDVI_{min}$ is the $NDVI$ of the bare soil without plants and $NDVI_{max}$ is the $NDVI$ of the full
133 vegetation cover, R_{nir} is the near-infrared reflectance and R_{red} is the red reflectance. The daily
134 reflectance R_{nir} and R_{red} were measured by MODIS reflectance data MOD09CMG (Fig. 1). Based on
135 Tang et al. (2009), we set $NDVI_{min} = 0.22$ and $NDVI_{max} = 0.83$. Missing observation for the daily
136 MOD09CMG calculated $NDVI$ data was filled with the 16-day averaged $NDVI$ values in the
137 MOD13Q1 data product (Fig. 1).

138 The available energy Q ($W m^{-2}$), which is the sum of the latent heat flux and sensible heat flux (also
139 known as the net radiation minus soil heat flux) is also separated into the available energy for vegetation
140 transpiration, Q_{veg} ($W m^{-2}$) and Q_{soil} ($W m^{-2}$) for bare soil evaporation, which was expressed by Nishida
141 et al. (2003) as:

$$142 \quad Q = f_{veg}Q_{veg} + (1 - f_{veg})Q_{soil} \quad (4)$$

143 As satellites like Terra and Aqua provide instantaneous snapshot observations of the Earth only once
144 a day, a temporal scaling method is needed to convert instantaneous measurements into daily ET values.
145 Nishida et al. (2003) used satellite-based noon time instantaneous evaporation fraction (EF), defined as
146 the ratio of latent heat flux (ET) to available energy as daily EF ($EF = \frac{ET}{Q}$), multiplied the daily Q to
147 calculated daily ET based on the assumption that EF is constant over a day

$$148 \quad ET = EF Q \quad (5)$$

149 In the next section, we will detail how VISEA calculates the daily EF , and Q in Equation (5), and also
150 daily air and land surface temperatures.



151 2.1.1 Daily evaporation fraction calculation

152 Combining Eq. 1 and 4, we first calculated the instantaneous evaporation fraction, EF^i as:

$$153 \quad EF^i = f_{veg} \frac{Q_{veg}^i}{Q^i} EF_{veg}^i + (1 - f_{veg}) \frac{Q_{soil}^i}{Q^i} EF_{soil}^i \quad (6)$$

154 where the superscript i stands for the instantaneous value of the parameter, EF_{veg}^i and EF_{soil}^i are the
 155 instantaneous full vegetation coverage and bare soil EF , respectively. EF_{veg}^i can be expressed as a
 156 function of instantaneously parameters as (Nishida et al., 2003):

$$157 \quad EF_{veg}^i = \frac{\alpha \Delta^i}{\Delta^i + \gamma(1 + r_{c,veg}^i / 2r_{a,veg}^i)} \quad (7)$$

158 where α is the Priestley-Taylor parameter, which was set to 1.26 for wet surfaces (De Bruin, 1983); Δ^i is
 159 the slope of the saturated vapor pressure, which is a function of the temperature (Pa K⁻¹); γ is the
 160 psychrometric constant (Pa K⁻¹); $r_{c,veg}^i$ is the instantaneous surface resistance of the vegetation canopy (s
 161 m⁻¹); $r_{a,veg}^i$ is the instantaneous aerodynamics resistance of the vegetation canopy (s m⁻¹). EF_{soil}^i was
 162 expressed by Nishida et al. (2003) as a function of the instantaneous soil temperature and the available
 163 energy based on the energy budget of the bare soil:

$$164 \quad EF_{soil}^i = \frac{T_{soil,max}^i - T_{soil}^i}{T_{soil,max}^i - T_a^i} \frac{Q_{soil0}^i}{Q_{soil}^i} \quad (8)$$

165 where $T_{soil,max}^i$ is the instantaneous maximum possible temperature at the surface reached when the land
 166 surface is dry (K), T_{soil}^i is the instantaneous temperature of the bare soil (K), T_a^i is the instantaneous air
 167 temperature, Q_{soil0}^i is the instantaneous available energy when T_{soil}^i is equal to T_a^i (W m⁻²).

168
 169 As the assumption of $EF^i = EF^d$ caused 10%-30% underestimation of daily ET (Huang et al.,
 170 2017; Yang et al., 2013), we introduced a decoupling parameter to convert EF^i into EF^d following the
 171 algorithm of Tang et al. (2017a, 2017b). This new decoupling parameter-based evaporation fraction is
 172 developed from Penman-Monteith and McNaughton-Jarvis mathematical equations:

$$173 \quad EF^d = EF^i \frac{\Delta^d}{\Delta^d + \gamma} \frac{\Delta^i + \gamma}{\Delta^i} \frac{\Omega^i}{\Omega^d} \frac{\Omega^d}{\Omega^i} \quad (9)$$

174 where superscript "d" means daily; the EF^i is the instantaneous evaporation fraction; Ω is the decoupling
 175 factor that represents the relative contribution of radiative and aerodynamic terms to the overall
 176 evapotranspiration (Tang and Li, 2017), Ω_i^* is the value of the decoupling factor, Ω , for wet surfaces.
 177 According to Pereira (2004), Ω and Ω^* can be expressed as:

$$178 \quad \Omega = \frac{1}{1 + \frac{\gamma}{\Delta + \gamma r_a}} \quad (10)$$

$$179 \quad \Omega^* = \frac{1}{1 + \frac{\gamma}{\Delta + \gamma r_a}} \quad (11)$$

$$180 \quad r^* = \frac{(\Delta + \gamma) \rho C_p VPD}{\Delta \gamma (R_n - G)} \quad (12)$$



181 where r_c is the surface resistance ($s\ m^{-1}$); r_a is the aerodynamic resistance ($s\ m^{-1}$); the calculation details
 182 of instantaneous and daily r_c and r_a for vegetation and soil are explained in Appendix A. r^* is the critical
 183 surface resistance when the actual evapotranspiration equals the potential evaporation (called equilibrium
 184 evapotranspiration, $s\ m^{-1}$); ρ is the air density ($kg\ m^{-3}$); C_p is the specific heat of the air ($J\ kg^{-1}\ K^{-1}$); VPD
 185 is the vapor pressure deficit of the air (Pa). Δ is the slope of the saturated vapor pressure ($Pa\ K^{-1}$).

186 For full vegetation-covered areas, EF_{veg}^d is expressed as:

$$187 \quad EF_{veg}^d = \frac{\alpha \Delta^i}{\Delta^{i+\gamma} \left(1 + \frac{r_c^i}{2r_a^i}\right)} \left(\frac{\Delta^d}{\Delta^{d+\gamma}} \frac{\Delta^{i+\gamma} \Omega_{veg}^{*i}}{\Delta^i \Omega_{veg}^{*d}} \frac{\Omega_{veg}^d}{\Omega_{veg}^i} \right) \quad (13)$$

188 For bare soil, EF_{soil}^d is:

$$189 \quad EF_{soil}^d = \frac{T_{soil\ max}^i - T_{soil}^i}{T_{soil\ max}^i - T_a^i} \frac{Q_{soil}^i}{Q_{soil}^d} \left(\frac{\Delta^d}{\Delta^{d+\gamma}} \frac{\Delta^{i+\gamma} \Omega_{soil}^{*i}}{\Delta^i \Omega_{soil}^{*d}} \frac{\Omega_{soil}^d}{\Omega_{soil}^i} \right) \quad (14)$$

190 Thus, EF^d is expressed as:

$$191 \quad EF^d = f_{veg} \frac{Q_{veg}^i}{Q^i} EF_{veg}^d + (1 - f_{veg}) \frac{Q_{soil}^i}{Q^i} EF_{soil}^d \quad (15)$$

192 2.1.2 Daily calculation of available energy Q_{veg}^d and Q_{soil}^d

193 The daily available energy Q ($W\ m^{-2}$) for the vegetation and the bare soil surface is calculated by
 194 the energy balance equation:

$$195 \quad R_n - G = Q \quad (16)$$

196 where R_n is the net radiation ($W\ m^{-2}$), which could be calculated by the land surface energy balance; G
 197 is the soil heat flux ($W\ m^{-2}$). ($G \approx 0$ on a daily basis),

$$198 \quad R_n^d = (1 - albedo^d) R_d^d - \varepsilon_s^d \sigma T_s^{d\ 4} + (1 + Cloud^d) \varepsilon_a^d \sigma T_a^{d\ 4} \quad (17)$$

199 where $albedo^d$ is the daily albedo of the soil surface; R_d^d is daily incoming shortwave radiation ($W\ m^{-2}$);
 200 ε_s^d and ε_a^d are the daily emissivity of land surface and atmosphere (Brutsaert, 1975; Wang and Dickinson,
 201 2013; details are presented in Appendix B), ε_s^d can be retrieved by MOD11C1; σ is the Stefan-Boltzmann
 202 constant; T_a^d is the daily near surface air temperature (K); T_s^d is the daily surface temperature (K).

203 For the downward longwave radiation, we account for the influence of clouds by assuming a linear
 204 correlation between downward longwave radiation and cloud coverage:

$$205 \quad Cloud = (1 - K_t) \quad (18)$$

$$206 \quad K_t = \frac{R_d^d}{R_a^d} \quad (19)$$



207 $Cloud^d$ is derived from the clearness index K_t (Chang and Zhang, 2019; Goforth et al., 2002). R_a^d is the
208 daily extraterrestrial radiation calculated by the FAO (1998).

209 According to Huang et al. (2021), Q_{veg}^d can be calculated by assuming as $T_s^d = T_a^d$ according to the
210 VI-Ts method which implies that the minimum land surface temperature occurs in fully vegetated grid
211 cells and is equivalent to T_a^d .

$$212 \quad Q_{veg}^d = (1 - albedo^d)R_a^d + (1 + Cloud^d)\epsilon_a^d \sigma T_a^{d4} - \epsilon_s^d \sigma T_s^{d4} \quad (20)$$

$$213 \quad Q_{soil}^d = (1 - C_G)(1 - albedo^d)R_a^d + (1 + Cloud^d)\epsilon_a^d \sigma T_a^{d4} - \epsilon_s^d \sigma T_s^{d4} \quad (21)$$

214 Thus, $(1 + Cloud^d)\epsilon_a^d \sigma T_a^{d4}$ is the daily downward longwave radiation ($W m^{-2}$), and $\epsilon_s^d \sigma T_s^{d4}$ is the
215 daily upward longwave radiation ($W m^{-2}$), where C_G is an empirical coefficient ranging from 0.3 for a
216 wet soil to 0.5 for a dry soil (Idso et al., 1975).

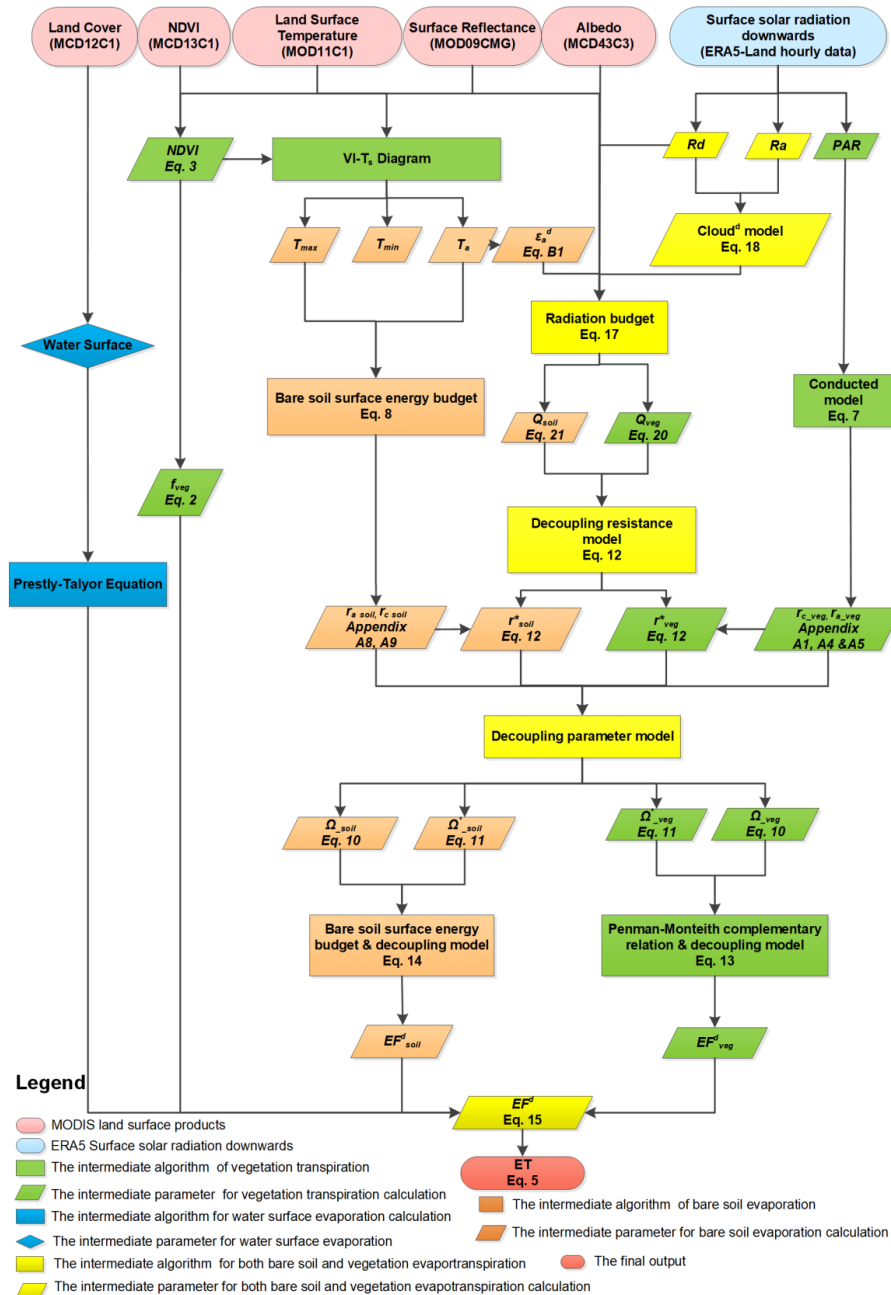
217

218 Following the study of Huang et al. (2021), the daily ET^d can be calculated by the daily EF^d and
219 Q^d as:

$$220 \quad ET^d = EF^d Q^d \quad (22)$$

221 Figure 1 illustrates the workflow of VISEA.

222



223

224 **Figure 1.** Schematic of VISEA algorithm. The ovals in the top row are the databases, and the square
 225 boxes are the algorithms, and parallelograms are the parameters. The numbers in the parenthesis are the
 226 equation to determine the parameters.

227



228 2.1.3 The calculation of daily air temperature, T_a^d and surface temperature, T_s^d

229 Daily air temperature, T_a^d is a critical parameter in the VISEA algorithm, used in calculations for
230 downward longwave radiation, daily aerodynamic resistance, and surface resistance. The key innovation
231 in calculating T_a^d , involves employing the VI-Ts method to estimate instantaneous air temperature, T_a^i
232 during the daytime. For nighttime periods, it is assumed that air temperature is equivalent to the nighttime
233 land surface temperature provided by MOD11C1. These two temperature estimates are then extended
234 into hourly air temperature profiles using a sine-cosine fitting curve. The 24-hour average of T_a^i is used
235 as T_a^d . Similarly, T_s^d is calculated using MOD11C1 land surface temperature data for both daytime and
236 nighttime. These estimates are extended into hourly surface temperature profiles using a similar sine-
237 cosine fitting curve, and the daily average of T_s^d is determined (Huang et al., 2021).

238 A key advance of this VISEA algorithm is the application of the VI-Ts method to calculate $T_{soil\ max}^i$
239 and T_a^i (Huang et al., 2017; Nishida et al., 2003; Tang et al., 2009). The VI-Ts method is based on the
240 empirical linear relationship between the vegetation index (VI), typically calculated by NDVI, and land
241 surface temperature (Ts). When plotted on a two-dimensional scatter plot, VI and Ts generally form a
242 trapezoid or triangular shape. In these plots, regions with low VI and high Ts values constitute the "warm
243 edge," while areas with high VI and low Ts values form the "cold edge." Using simple linear interpolation,
244 Ts values corresponding to any given VI between the "warm edge" and the "cold edge" can be determined.
245 Assuming $T_s = T_a^i$ for cases where the highest VI corresponds to the lowest Ts, we can calculate T_a^i .
246 Similarly, $T_{soil\ max}^i$ can be easily calculated since it corresponds to the lowest VI.

247 This VI-Ts method allows for the estimation of T_a^i and $T_{soil\ max}^i$ without the need for additional
248 meteorological data. However, it's worth noting that some studies have found that the VI-Ts method may
249 not consistently provide satisfactory results, especially in colder regions where vegetation thrives better
250 under higher temperatures.

251 2.2 Technical validation

252 The correlation coefficient, Root Mean Square Error (RMSE) and Nash-Sutcliffe efficiency coefficient
253 are used to evaluate our global daily ET estimates with eddy covariance measurements and compared
254 with the other five independent global ET products on a monthly scale.

255 The correlation coefficient R is calculated as:

$$256 \quad R = \frac{\sum(X-\bar{X})(Y-\bar{Y})}{\sqrt{\sum(X-\bar{X})^2 \sum(Y-\bar{Y})^2}} \quad (23)$$

257 R is the correlation coefficient; X is the estimated variable; \bar{X} is the average of X; Y is the observed
258 variable; \bar{Y} is the average of Y.

259 The Root Mean Square Error (RMSE) is calculated as:

$$260 \quad RMSE = \sqrt{\frac{\sum_{i=1}^N (X_i - Y_i)^2}{N}} \quad (24)$$



261 For a more nuanced understanding of the Root Mean Square Error (RMSE), we have deconstructed
262 it into two distinct components: RMSEs (systematic RMSE) and RMSEu (unsystematic RMSE). This
263 breakdown allows a more detailed examination of the systematic and unsystematic sources contributing
264 to the overall error metric.

265 The systematic Root Mean Square Error (RMSEs) is calculated as:

$$266 \quad RMSEs = \sqrt{\frac{\sum_{i=1}^N (Z_i - Y_i)^2}{N}} \quad (25)$$

267 The unsystematic Root Mean Square Error (RMSEu) is calculated as:

$$268 \quad RMSEu = \sqrt{\frac{\sum_{i=1}^N (Z_i - X_i)^2}{N}} \quad (26)$$

269 Where $Z_i = a + bY_i$, where a and b are the least squares regression coefficients of the estimated variable
270 X_i and observed variable Y_i , N is the sample size (Norman et al., 1995).

271 The Nash-Sutcliffe efficiency coefficient (NSE)

$$272 \quad NSE = 1 - \frac{\sum_{i=1}^N (X_i - Y_i)^2}{\sum_{i=1}^N (Y_i - \bar{Y})^2} \quad (27)$$

273 The ratio of the standard deviations of X and Y

$$274 \quad Ratio = \frac{X_{Standard\ Deviation}}{Y_{Standard\ Deviation}} \quad (28)$$

275 The Bias of X and Y

$$276 \quad Bias = \bar{X} - \bar{Y} \quad (29)$$

277 2.3 The gap-filling of MODIS data

278 MODIS sensors on board of Terra and Aqua observe the Earth twice a day. However, there are
279 always data gaps in the MODIS land products because of cloud cover problems. In the VISEA algorithm,
280 we used the neighboring days' available data to fill the data gaps. According to the study of Tang et al.
281 (2009), the cloud gaps don't reduce the accuracy of this algorithm significantly.

282 3. Data

283 3.1 The input data

284 The input data including the MODIS land products: daily 0.05° surface reflectance (MOD09CMG),
285 land surface temperature/emissivity (MOD11C1) and albedo (MCD43C3), 8-day 0.05° vegetation
286 indices (MOD13C1) and yearly 0.05° land cover products (MCD12C1). We also used hourly downward
287 surface solar radiation from the Fifth Generation of the European Centre for Medium-Range Weather



288 Forecasts (ECMWF) Reanalysis (ERA5), “ERA5-Land hourly data from 1950 to present” data as energy
289 input of VISEA algorithm. The surface solar radiation data from ERA5-Land and land data products from
290 MODIS land products are both near-real-time datasets with a one-week delay, enabling VISEA to provide
291 global near-real-time ET estimations. Details of the input data, their download links, variable names, used
292 parameters, spatial and temporal resolution are given in Table 1.

293 **Table 1. The input of VISEA**

The input of VISEA			
Data source	Data name	Used parameter	Spatial/temporal resolution
MODIS Land Product	MOD11C1	Land Surface Temperature	0.05°/ daily
	MOD09CMG	Surface Reflectance	0.05°/daily
	MCD43C3	Albedo	0.05°/daily
	MOD13C1	NDVI	0.05°/16-day
	MCD12C1	Land cover	0.05°/ yearly
ERA5-Land hourly data	Rd	Downward surface solar radiation	0.1°/ hourly

294

295 **3.2 The evaluation data**

296 **3.2.1 The flux tower measurements from FLUXNET**

297 We evaluated the accuracy of daily averaged ERA5-Land shortwave radiation, VISEA estimated daily
298 net radiation, air temperature and ET by comparing them with measurements from FLUXNET2015 flux
299 towers FLUXNET2015: CC-BY-4.0 (Pastorello et al., 2020) (<https://fluxnet.org/data/download-data/>).
300 we compared its results with measurements obtained from FLUXNET2015: CC-BY-4.0 15, which can
301 be accessed at <https://fluxnet.org/data/download-data/>. While there are records from a total of 212 flux
302 towers in our datasets, not all of them met our stringent inclusion criteria. Each site needed to fulfill three
303 specific requirements to be included in our analysis: (1) availability of data for the period spanning from
304 2001 to 2015; (2) ERA5-Land downward shortwave radiation greater than 0 within the $0.1^\circ \times 0.1^\circ$ grid
305 cell corresponding to the flux tower's location; (3) conformity with MODIS land cover data (MOD12C1)
306 at the $0.05^\circ \times 0.05^\circ$ grid cell level, ensuring that the flux tower was situated on land rather than over the
307 ocean.

308 As a result, our study incorporates data from a carefully selected subset of 149 flux towers that met
309 these stringent criteria. This approach ensures the reliability and relevance of our analysis. The
310 distribution of these 149 flux towers is presented in Figure 2. Supplementary Table S1 shows the
311 longitude, latitude, elevation, and land cover type (classified by the International Geosphere-Biosphere
312 Programme, IGBP) of these sites. The 149 sites covered 12 IGBP land cover types: 18 croplands (CRO),
313 1 closed shrublands (CSH), 15 deciduous broadleaf forests (DBF), 1 deciduous needle leaf forest (DNF),
314 10 evergreen broadleaf forests (EBF), 34 evergreen needle leaf forests (ENF), 30 grasslands (GRA), 5
315 mixed forests (MF), 8 open shrublands (OSH), 8 savannas (SAV), 13 wetlands (WET), and 6 woody
316 savannas (WSA).



317 **3.2.2 The other gridded ET and precipitation products**

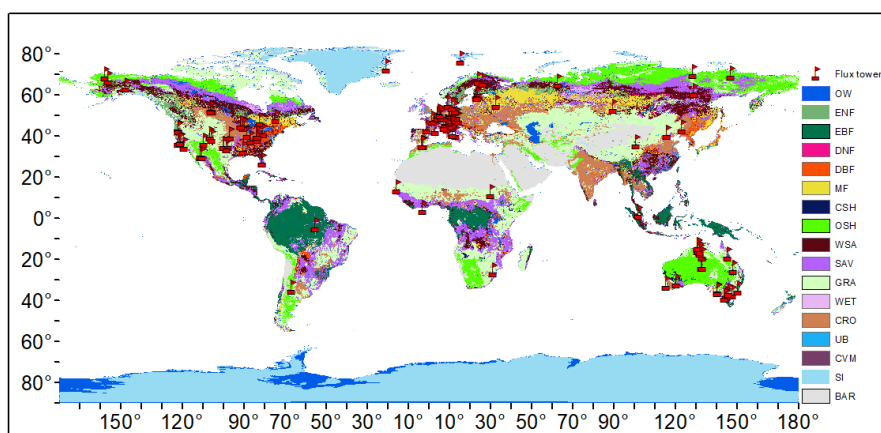
318 We also used five independent globally gridded ET and one precipitation products for VISEA estimated
 319 ET's comparison. The five ET products include two MODIS-based ET products: MOD16 (Mu et al.,
 320 2007, 2011) and Penman-Monteith-Leuning Evapotranspiration V2 (PML) (Zhang et al., 2019, 2022),
 321 one AVHRR-based AVHRR ET (Zhang et al., 2009, 2010), one machine learning algorithm output, the
 322 Global Bio-Atmosphere Flux (GBAF) (Jung et al., 2009, 2010, 2018, 2019) and one multiple-satellites
 323 data based Global Land Evaporation Amsterdam Model (GLEAM) ET (Martens et al., 2017; Miralles et
 324 al., 2011). The precipitation data was from the Global Precipitation Climatology Centre (GPCC), which
 325 is based on local measurements (Schneider et al., 2014, 2017; Becker et al., 2013) and Global Unified
 326 Gauge-Based Analysis of Daily Precipitation (GPC). Details of these five ET products and the
 327 precipitation data are given in Table 2. To maintain the consistency in temporal and spatial resolution for
 328 comparison purposes, we obtained monthly MOD16 and PML, despite their original temporal resolution
 329 of 8 days and used the 0.05°×0.05° version of MOD16, AVHRR ET and PML.

330 **Table 2.** The five global girded ET products and one precipitation product used for comparison with our
 331 near-real-time global daily terrestrial ET estimates.

Product name	Spatial/Temporal resolution	Time period	Theory
GLEAM	0.25°/Monthly	2002-2019	Priestly-Taylor Equation
GBAF	0.5°/Monthly	2001-2008	Machine learning
MOD16	0.05°/8-day	2001-2013	Penman-Monteith Equation
AVHRR	1°/Monthly	2001-2006	Improved Penman-Monteith Equation
PML	0.05°/8-day	2003-2018	Penman-Monteith Equation and a diagnostic biophysical model
GPCC	0.25°/Monthly	2001-2019	in-situ observations
GPC	0.5°/Daily	08/28/2022-09/01/2022	Global Unified Gauge-Based Analysis of Daily Precipitation

332

333



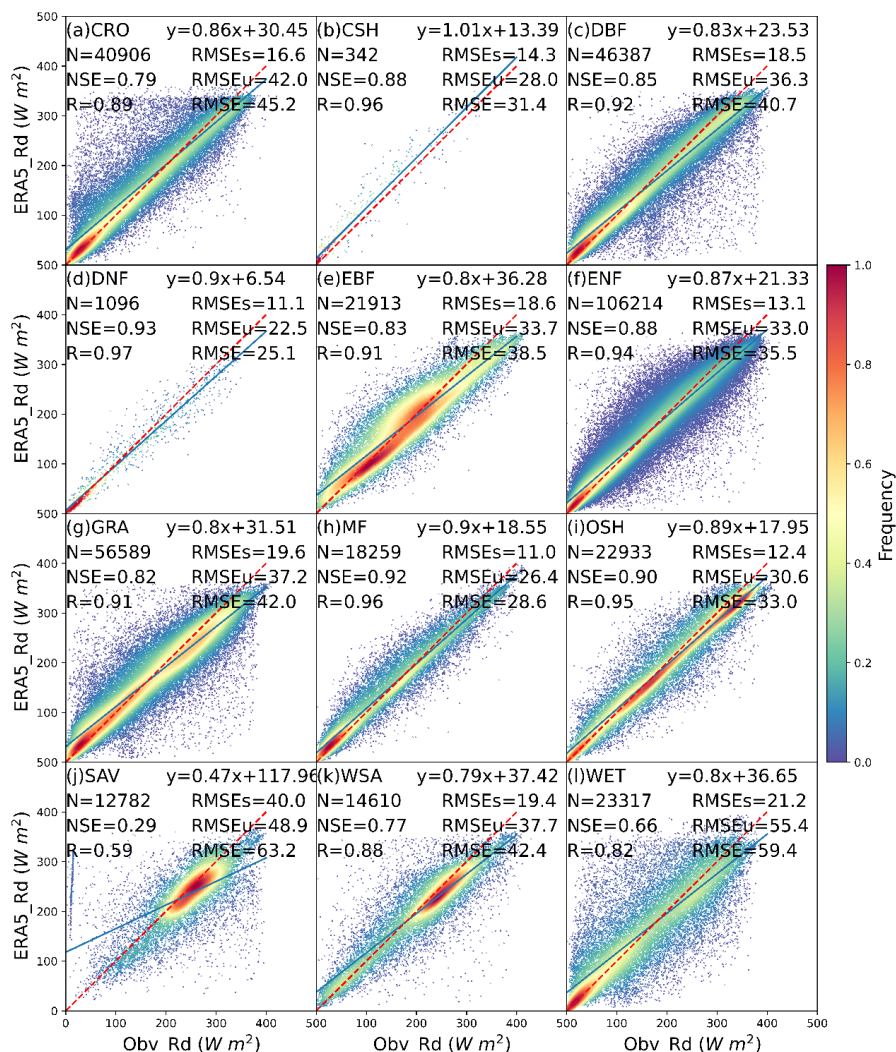
334

335 **Figure 2.** The distribution of 149 flux towers from FLUXNET in different IGBP land cover types,
336 specifically OW (Water bodies), ENF (Evergreen needle leaf forests), EBF (Evergreen broadleaf forests),
337 DNF (Deciduous needle leaf forests), DBF (Deciduous broadleaf forests), MF (Mixed forests), CSH
338 (Closed shrublands), OSH (Open shrublands), WSA (Woody savannas), SAV (Savannas), GRA
339 (Grasslands), WET (Permanent wetlands), CRO (Croplands), UB (Urban and built-up lands), CVM
340 (Cropland/natural vegetation mosaics), SI (Snow and ice), BAR (Barren).

341 4. Results

342 In our initial analysis, we juxtaposed downward solar radiation input data from ERA5-Land
343 (ERA5_Rd) with measurements obtained from 149 flux towers (Obv_Rd) across diverse IGBP land cover
344 types, as illustrated in Figure 3. The results indicate a commendable agreement between ERA5_Rd and
345 Obv_Rd measurements for the majority of land covers, with notable exceptions observed in savanna
346 (SAV). Specifically, the mean Nash-Sutcliffe Efficiency (NSE) stands at 0.84, the mean correlation
347 coefficient (R) at 0.92, and the mean Root Mean Square Error (RMSE) at 38.3 W m^{-2} . This comparative
348 analysis offers helpful insights into the performance of ERA5_Rd across different land cover categories.

349 In Figure 3, ERA5_Rd exhibits optimal performance in DNF and MF, reflected by NSE and R values
350 surpassing 0.9. In these land covers, the mean RMSEs stand at 11 W m^{-2} , mean RMSEu at 24.5 W m^{-2} ,
351 and mean RMSE at 26.9 W m^{-2} . However, its performance in SAV is notably subpar, characterized by
352 an NSE of 0.29, an R of 0.59, highest RMSEs of 40 W m^{-2} , RMSEu of 48.9 W m^{-2} , and RMSE of 63.2
353 W m^{-2} . For ERA5_Rd, the mean RMSEs amount to 16 W m^{-2} , and the mean RMSEu is 34.8 W m^{-2} ,
354 suggesting that ERA5_Rd demonstrates high accuracy by effectively capturing the systematic variation
355 in Obv_Rd, as indicated by its relatively low RMSEs and RMSEu close to RMSE (Willmott et al., 1981)
356 in most land covers, except for SAV.



357

358 **Figure 3.** The scatter plot of downward solar radiation from ERA5-Land (ERA5_Rd) compared
 359 with local instruments measurements (Obsv_Rd) under 12 IGBP land cover types: CRO (Croplands), CSH
 360 (Closed shrublands), DBF (Deciduous broadleaf forests), DNF (Deciduous needle leaf forests), EBF
 361 (Evergreen broadleaf forests), ENF (Evergreen needle leaf forests), GRA (Grasslands), MF (Mixed
 362 forests), OSH (Open shrublands), SAV (Savannas), WSA (Woody savannas), WET (Permanent
 363 wetlands). The red dotted line is the 1:1 line. N is the number of data points, NSE is Nash-Sutcliffe
 364 Efficiency, R is correlation coefficients, RMSE is Root Mean Square Error, RMSEs is systematic RMSE,
 365 and RMSEu is unsystematic RMSE.

366 Several factors come into play in understanding the disparities in performance in downward solar
 367 radiation of ERA5 (ERA5_Rd) across different land cover types. In regions characterized by denser
 368 forests, such as DNF and MF, ERA5_Rd's superior performance may be attributed to the lower density

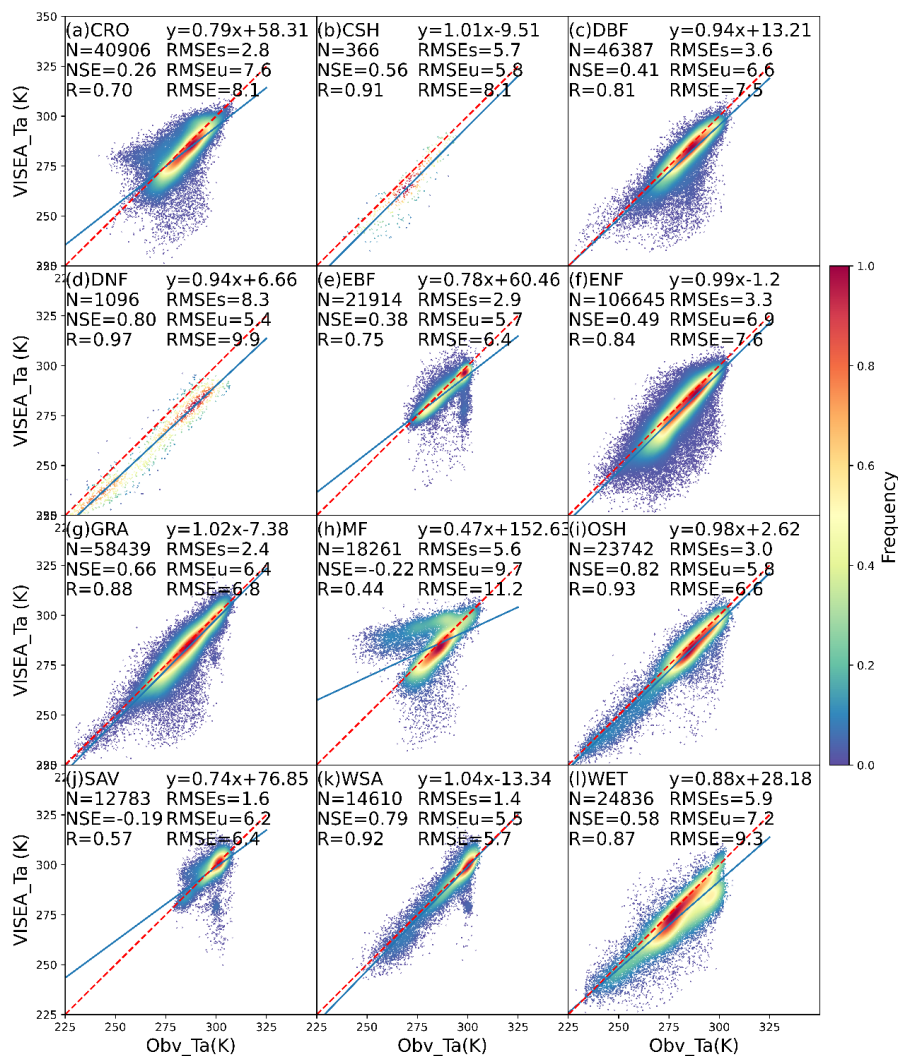


369 of ground-based meteorology stations (DNF, $N = 1096$) and the relatively uniform subsurface and canopy
370 coverage in MF, facilitating a more accurate representation in the ERA5 radiative transfer model.
371 Conversely, savannas present unique challenges due to sparse vegetation and flat terrain, influencing
372 sunlight transmission dynamics (Yang and Friedl, 2003). Land-use changes, including farming and urban
373 development, further complicate the accuracy of sunlight transmission (Wang et al., 2014; Zhang et al.,
374 2022). Additionally, factors like aerosols from natural or anthropogenic sources contribute to data
375 variations (Naud et al., 2014; Wang et al., 2021). The inaccuracies in accounting for the rainy season,
376 leading to increased cloud cover and rainfall in savannas, contribute to ERA5_Rd's limitations (Jiang et
377 al., 2020).

378 Figure 4 depicts scatter plots illustrating the comparison between the estimated air temperature using
379 the VI-T_s method (VISEA_Ta) and local meteorological measurements (Obv_Ta). The analysis reveals
380 that VISEA_Ta generally aligns with Obv_Ta, exhibiting NSE values ranging from -0.22 (MF) to 0.82
381 (OSH), R values ranging from 0.44 (MF) to 0.97 (DNF), and RMSE values ranging from 5.7 K (WSA)
382 to 11.2 K (MF). Particularly noteworthy is VISEA_Ta's outstanding performance at OSH (NSE = 0.82,
383 R = 0.93, RMSE = 6.6 K), WSA (NSE = 0.79, R = 0.92, RMSE = 5.7 K) and GRA (NSE = 0.66, R =
384 0.88, RMSE = 6.8 K).

385 Conversely, its least satisfactory performance is evident at MF (NSE = -0.22, R = 0.44, RMSE =
386 11.2 K), SAV (NSE = -0.19, R = 0.57, RMSE = 6.4 K), and CRO (NSE = 0.26, R = 0.70, RMSE = 8.1
387 K). The RMSEs are lower than RMSE_{Eu} in most land cover sites, except in DNF. Despite VISEA_Ta
388 displaying a high NSE of 0.8 and R of 0.97 at DNF, it exhibits higher RMSEs (8.3 K) compared to
389 RMSE_{Eu} (5.4 K), indicating a systematic underestimation of VISEA_Ta at DNF.

390 As detailed in Section 2.4, the VI-T_s method relies on a negative correlation between vegetation
391 coverage (VI) and land surface temperature (T_s), ideally suited for cases with significant VI and T_s
392 differences. However, for land cover types like DNF and MF situated in temperate regions with distinct
393 seasons and cool to cold climates, the assumed negative correlation breaks down. In these regions, the
394 positive correlation between VI and T_s, driven by vegetation growth proportional to rising T_s, results in
395 the failure of the VI-T_s method. The challenges persist in SAV, where the VI-T_s method encounters
396 difficulties during both dry and wet seasons. In the dry season, the method falters due to the prevalence
397 of bare soil, resulting in VI values approaching zero and homogeneous high T_s values. Conversely, the
398 wet season presents challenges with both VI and T_s exhibiting relatively high values and limited
399 variances between grid cells, ultimately undermining the accuracy of VISEA_Ta estimation.



400

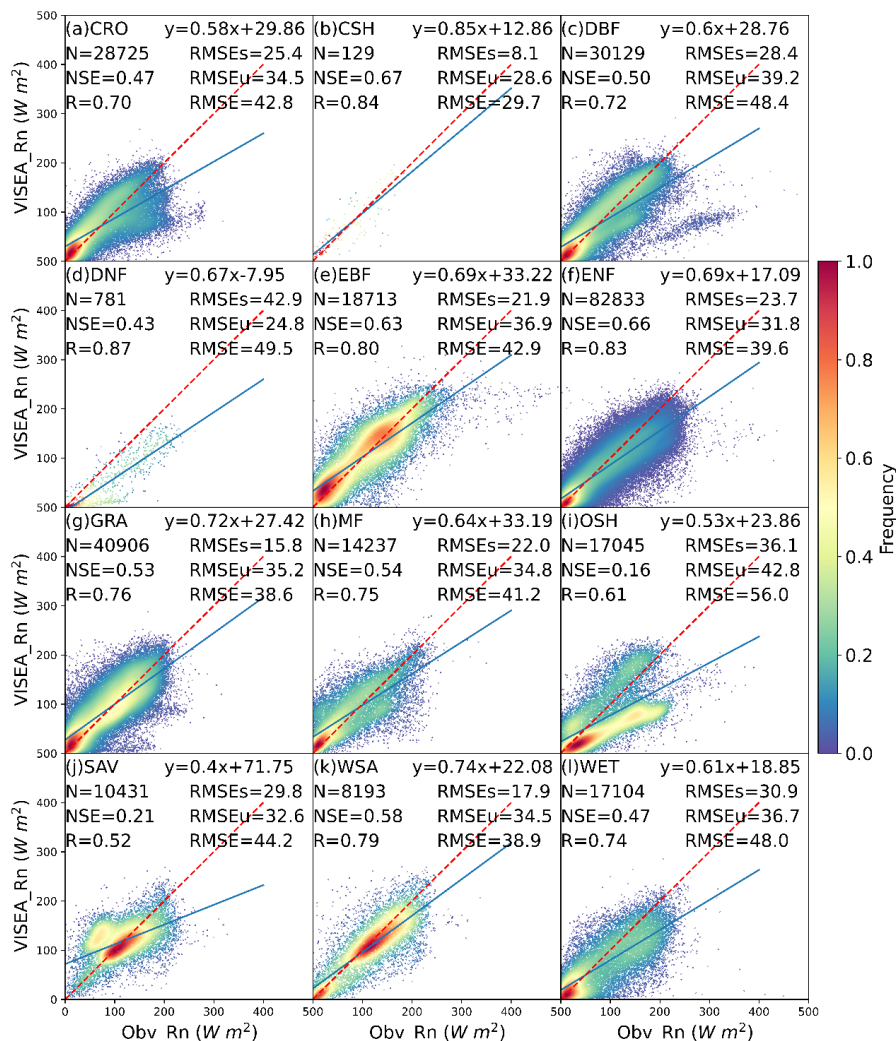
401 **Figure 4.** The scatter plot of daily air temperature simulated by VISEA (VISEA_Ta) compared with local
 402 instruments measurements (Obv_Ta) under 12 IGBP land cover types: CRO (Croplands), CSH (Closed
 403 shrublands), DBF (Deciduous broadleaf forests), DNF (Deciduous needle leaf forests), EBF (Evergreen
 404 broadleaf forests), ENF (Evergreen needle leaf forests), GRA (Grasslands), MF (Mixed forests), OSH
 405 (Open shrublands), SAV (Savannas), WSA (Woody savannas), WET (Permanent wetlands). The red
 406 dotted line is the 1:1 line. N is the number of data points, NSE is Nash-Sutcliffe Efficiency, R is
 407 correlation coefficients, RMSE is Root Mean Square Error, RMSEs is systematic RMSE, and RMSEu is
 408 unsystematic RMSE.

409

The simulated daily net radiation (VISEA_Rn) from VISEA is assessed against local meteorological
 410 measurements (Obv_Rn) in Figure 5. In contrast to the satisfactory performance of ERA5_Rd in Figure
 411 3, VISEA_Rn exhibits more notable discrepancies, characterized by significant underestimation



412 compared to Obv_Rn. This is reflected in the mean NSE of 0.49, mean R of 0.74, and mean RMSE of
 413 43.3 W m⁻².



414
 415 **Figure 5.** The scatter plot of daily net radiation simulated by VISEA (VISEA_Rn) compared with local
 416 instruments measurements (Obv_Rn) under 12 IGBP land cover types: CRO (Croplands), CSH (Closed
 417 shrublands), DBF (Deciduous broadleaf forests), DNF (Deciduous needle leaf forests), EBF (Evergreen
 418 broadleaf forests), ENF (Evergreen needle leaf forests), GRA (Grasslands), MF (Mixed forests), OSH
 419 (Open shrublands), SAV (Savannas), WSA (Woody savannas), WET (Permanent wetlands). The red
 420 dotted line is the 1:1 line. N is the number of data points, NSE is Nash-Sutcliffe Efficiency, R is
 421 correlation coefficients, RMSE is Root Mean Square Error, RMSEs is systematic RMSE, and RMSEu is
 422 unsystematic RMSE.



423 Specifically, VISEA_Rn demonstrates good accuracy in certain land cover types, including CHS
424 with an NSE of 0.67, R of 0.84, and RMSE of 29.7 W m⁻², EBF with an NSE of 0.63, R of 0.8, and RMSE
425 of 42.9 W m⁻², and ENF with an NSE of 0.66, R of 0.83, and RMSE of 39.6 W m⁻². However, its
426 performance diminishes notably at OSH, where it records an NSE of 0.16, R of 0.61, and RMSE of 56
427 W m⁻², as well as in SAV, with an NSE of 0.21, R of 0.52, and RMSE of 44.2 W m⁻².

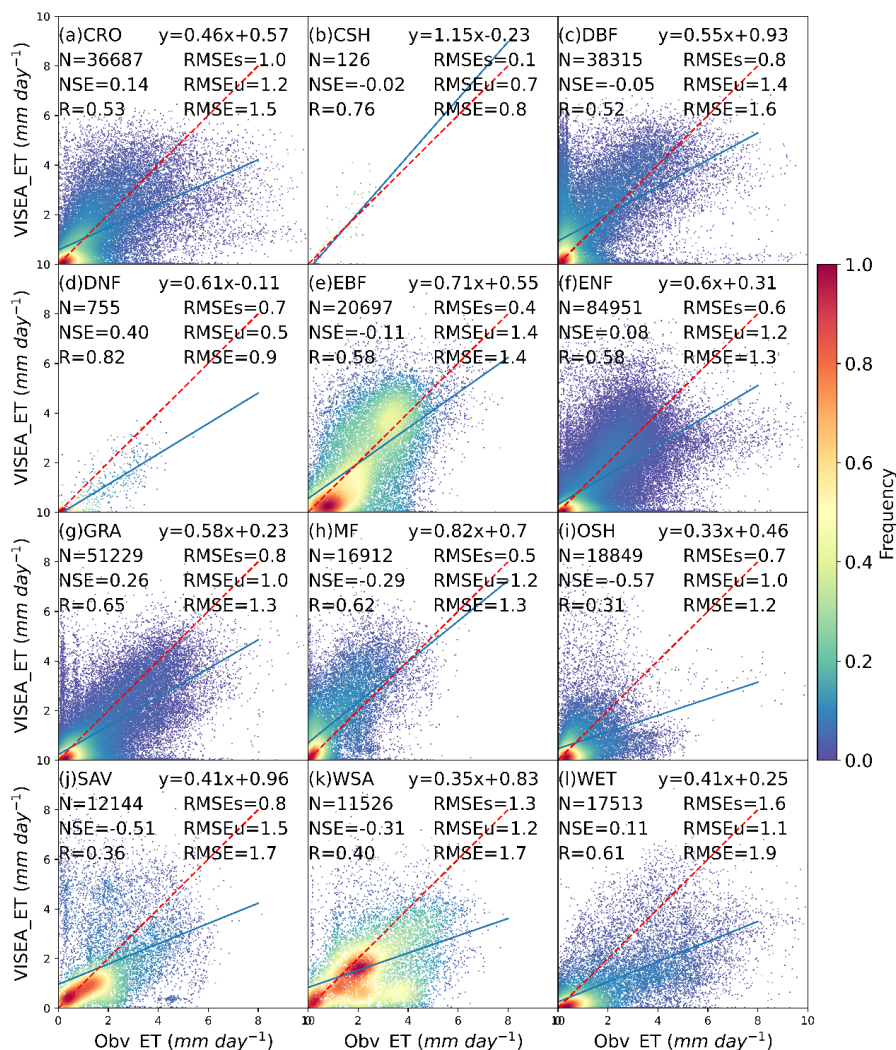
428 While VISEA_Rn appears to have lower accuracy compared to ERA5_Rd, in the majority of land
429 cover types, the RMSEs are smaller than RMSEu, with mean RMSEs of 25.2 W m⁻² and mean RMSEu
430 of 34.3 W m⁻². Moreover, the RMSEu of 43.3 W m⁻² is almost the same as the RMSE. These findings
431 suggest that VISEA_Rn demonstrates fewer systematic biases, with unsystematic RMSEu contributing
432 the most to the overall RMSE.

433 In the context of VISEA_Rn, a consistent pattern of approximately 30% underestimation in net
434 radiation across various land cover types raises noteworthy discussions. This systematic discrepancy
435 could be linked to the disparity in vegetation coverage between the observed sites' footprint and the mean
436 vegetation coverage of the 0.05° × 0.05° grid cell. Specifically, the lower albedo within the footprint,
437 compared to the grid cell's average albedo (as expressed by Eq. 20, contributes to the underestimation of
438 Obv_Rn. This is particularly evident in OSH, where the vegetation coverage within the footprint
439 significantly exceeds the mean vegetation coverage of the grid cell (<0.2 compared to >0.5).

440 Additionally, factors such as the bias in ERA5_Rd (refer to Fig. 3, j) and VISEA_Ta (refer to Fig.
441 4, j) contribute to the underestimation of VISEA_Rn in SAV. Moreover, a substantial 50%
442 underestimation in DNF results from the underestimated VISEA_Ta (refer to Fig. 4, d), leading to a
443 subsequent underestimation of downward long-wave radiation. Unpacking these intricacies sheds light
444 on the nuanced interplay of variables influencing the observed underestimation trends in VISEA_Rn
445 across diverse land cover types.

446 Figure 6 illustrates scatter plots of daily evapotranspiration (ET) simulated by VISEA (VISEA_ET)
447 against eddy covariance measurements obtained from 149 flux tower sites (Obv_ET) across 12 IGBP
448 land cover types. The scatter plots of VISEA_ET reveal a dispersed distribution, as evidenced by an
449 average NSE of -0.08, average R of 0.56, and average RMSE of 1.4 mm day⁻¹. Notably, VISEA_ET tends
450 to underestimate daily ET across most land cover types.

451 Among the 12 land cover types, VISEA_ET exhibits the highest accuracy in DNF, with an NSE of
452 0.4, an R of 0.82, and an RMSE of 0.9 mm day⁻¹. It was closely followed by GRA, with NSE values of
453 0.26, R values of 0.65, and RMSE values of 1.3 mm day⁻¹. However, for CRO, ENF, and WET land cover
454 types, the NSE values, although above 0, are close to 0 (mean NSE of 0.11), with a mean R of 0.53 and
455 a mean RMSE of 1.3 mm day⁻¹. In the remaining land cover types, particularly in OSH and SAV,
456 VISEA_ET appears to struggle in aligning with local measurements, resulting in NSE values of -0.57
457 and -0.51, R values of 0.31 and 0.36, and RMSE values of 1.2 mm day⁻¹ and 1.7 mm day⁻¹, respectively.



458

459 **Figure 6.** The scatter plot of daily ET simulated by VISEA (VISEA_ET) compared with local instruments
 460 measurements (Obsv_ET) under 12 IGBP land cover types: CRO (Croplands), CSH (Closed shrublands),
 461 DBF (Deciduous broadleaf forests), DNF (Deciduous needle leaf forests), EBF (Evergreen broadleaf
 462 forests), ENF (Evergreen needle leaf forests), GRA (Grasslands), MF (Mixed forests), OSH (Open
 463 shrublands), SAV (Savannas), WSA (Woody savannas), WET (Permanent wetlands). The red dotted line
 464 is the 1:1 line. N is the number of data points, NSE is Nash-Sutcliffe Efficiency, R is correlation
 465 coefficients, RMSE is Root Mean Square Error, RMSEs is systematic RMSE, and RMSEu is
 466 unsystematic RMSE.

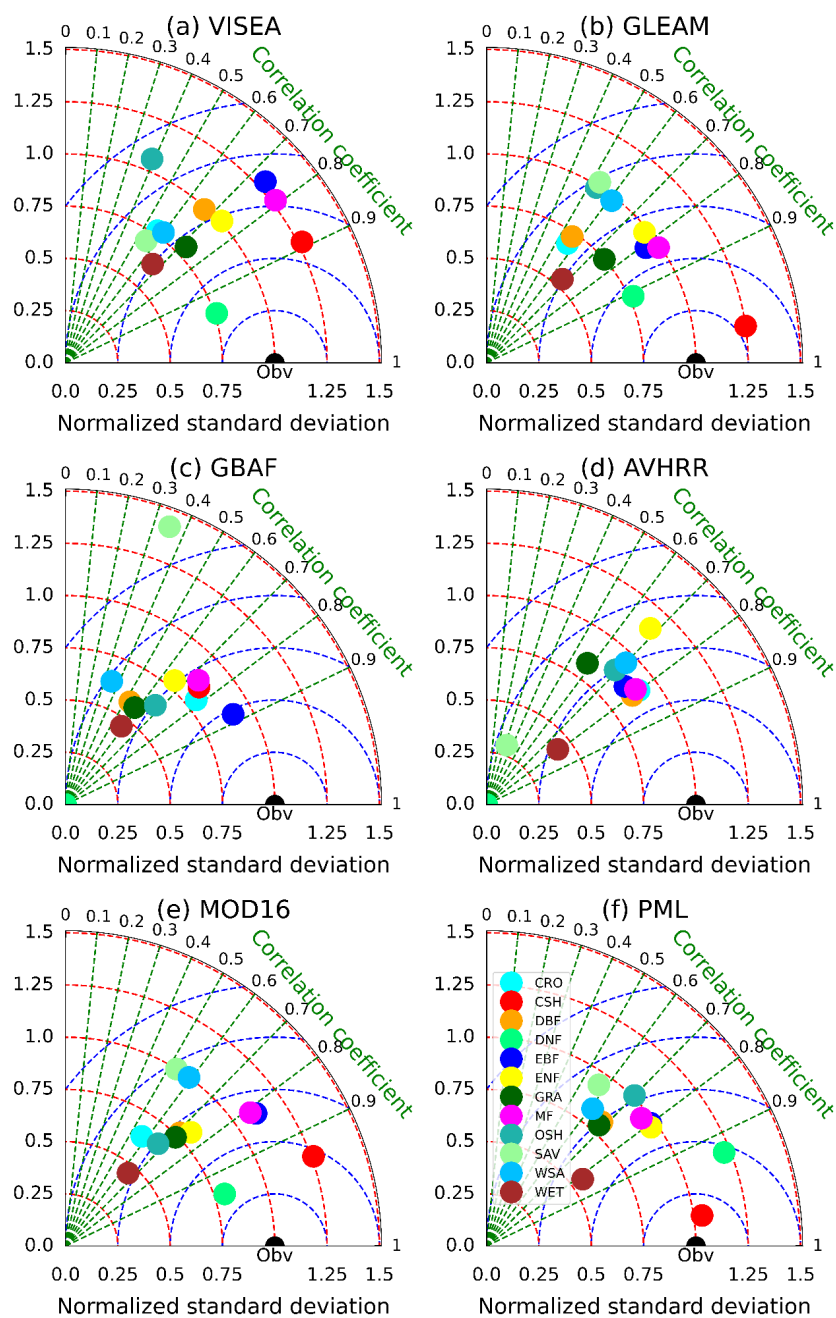
467 As the evaluation of daily VISEA_ET with observed ET, Obsv_ET, at CRO and WET, the bias
 468 mainly come from the bias in ERA5_Rd (the third highest RMSE of 45.2 W m^{-2} and second highest
 469 RMSE of 59.4 W m^{-2}) (Fig. 3, a and l). In ENF, the biases primarily could by the disability of VISEA_ET



470 to capturing the Obv_ET under a cold climate, with low net radiation estimation (Fig. 5, f), and air
471 temperature (Fig. 4, f). For OSH, the bias mainly arises from the poor estimation of VISEA_Rn, which
472 has the lowest NSE of 0.16 and highest RMSE of 56 W m^{-2} (Fig. 5, i). The bias of VISEA_ET in SAV is
473 a result of the combined biases in ERA5_Rd (the lowest NSE and R of 0.29 and 0.59, respectively, and
474 the highest RMSE of 63.2 W m^{-2}), VISEA_Ta (the second lowest NSE and R of -0.19 and 0.57 ,
475 respectively).

476 In Figure 7, we utilized Taylor diagrams (Taylor, 2001) to evaluate the performances of six global
477 gridded monthly ET products with simulated ET from VISEA (a), GLEAM (b), GBAF (c), AVHRR (d),
478 MOD16 (e), and PML (f). The statistical values, including correlation coefficient (CC), bias, RMSE,
479 RMSEu, RMSEs, and NSE are presented in Table 3. In contrast to the daily evaluation of VISEA, the
480 assessment on a monthly scale revealed significant performance metrics for VISEA, featuring a robust
481 mean correlation coefficient (CC) of 0.69, a mean Nash-Sutcliffe Efficiency (NSE) of 0.25, and the
482 highest mean Ratio of 0.94. On the downside, VISEA exhibited the highest mean bias, signifying an
483 underestimation of $-9.7 \text{ mm month}^{-1}$ and a moderate mean RMSE of $31.5 \text{ mm month}^{-1}$. Comparatively,
484 MOD16 has slightly better performance than VISEA with the second highest CC of 0.72 and higher NSE
485 of 0.41, lower bias of $-8.3 \text{ mm month}^{-1}$ and RMSE of $28.7 \text{ mm month}^{-1}$.

486 In contrast, GLEAM and PML stood out as top performers among all products. GLEAM displays
487 the second-highest CC of 0.71, a mean NSE of 0.39 and the lowest mean bias at $2.3 \text{ mm month}^{-1}$. While,
488 it also exhibited the highest mean RMSE of $31.5 \text{ mm month}^{-1}$ among the products. On the other hand,
489 PML achieved the highest mean CC of 0.75 and the highest NSE of 0.49 coupled with the lowest RMSE
490 at $25.9 \text{ mm month}^{-1}$ affirming its relatively accurate estimations. GBAF and AVHRR exhibit a higher
491 degree of disagreement with the observed data compared to the other ET products. GBAF presents the
492 lowest mean CC of 0.62, the second lowest NSE of 0.16, and an RMSE of $30.58 \text{ mm month}^{-1}$, while it
493 has the second lowest mean bias of $-4.3 \text{ mm month}^{-1}$, providing valuable insights into its performance
494 characteristics. On the other hand, AVHRR records the lowest NSE of 0.12, second lowest CC of 0.69
495 and the highest RMSE of $31.5 \text{ mm month}^{-1}$.



496

497 **Figure 7.** Taylor Diagrams comparing monthly measurements of (a) VISEA, GLEAM (b), GBAF (c),
 498 AVHRR (d), MOD16 (e), and PML (f) with 150 flux towers (labeled as Obsv) in different IGBP land
 499 cover types. The diagrams display the Normalized Standard Deviation (represented by red circles),
 500 Correlation Coefficient (shown as green lines), and Centred Root-Mean-Square (depicted as blue circles).



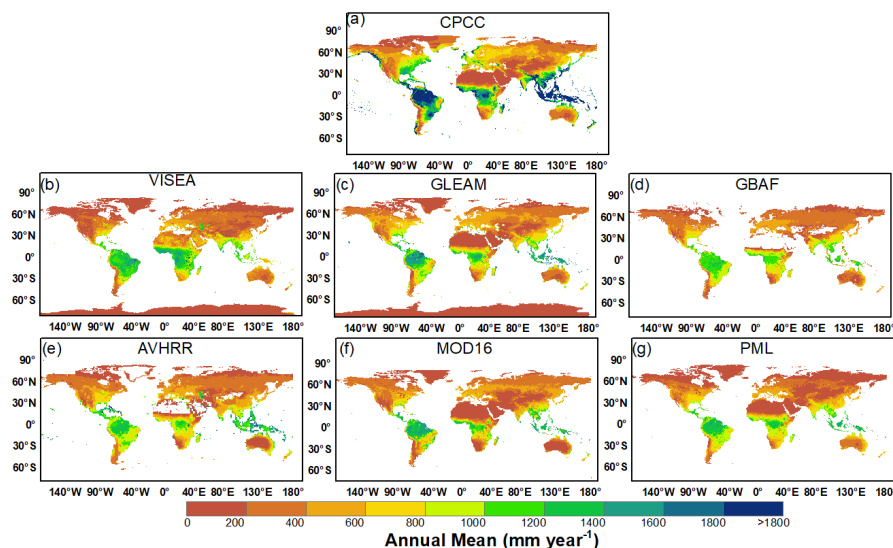
501 **Table 3.** Statistical variables of six ET Products – CC (Correlation Coefficient), Ratio (the ratio of the
 502 standard deviations of simulated ET and flux tower measurements), Bias, RMSE, RMSEu, RMSEs, and
 503 NSE.

		CRO	CSH	DBF	DNF	EBF	ENF	GRA	MF	OSH	SAV	WSA	WET	MEAN
WISEA	CC	0.57	0.89	0.67	0.95	0.74	0.74	0.72	0.79	0.39	0.55	0.6	0.66	0.69
	Ratio	0.77	1.27	0.99	0.76	1.29	1.01	0.8	1.27	1.06	0.7	0.78	0.63	0.94
	Bias	-14.16	-1.27	3.9	-19.06	1.37	-12.84	-13.47	1.53	-6.83	-0.45	-23.14	-31.98	-9.70
	RMSE	39.4	12.5	34	22.1	30.4	28.5	32	23.3	30.4	32.5	41.2	51.6	31.49
	RMSEU	27.4	12.1	30.7	7.4	30.4	23.8	23.1	23.2	25.4	22.5	25.8	25.4	23.10
	RMSES	28.3	3.1	14.5	20.8	2.2	15.7	22.2	1.5	16.8	23.5	32.1	44.9	18.80
	NSE	0.18	0.64	0.34	0.45	0.24	0.33	0.41	0.38	-0.36	0.28	0.01	0.08	0.25
GLEAM	CC	0.56	0.99	0.56	0.91	0.81	0.77	0.75	0.83	0.53	0.53	0.61	0.67	0.71
	Ratio	0.69	1.25	0.73	0.77	0.94	0.98	0.75	0.99	0.99	1.02	0.98	0.54	0.89
	Bias	-5.68	10.71	-3.55	-6.12	3.41	2.34	-2.01	10.67	4.44	-7.99	-17	-16.26	-2.25
	RMSE	36.8	12.1	35.8	14.6	21.4	23.8	27.6	20.2	25.6	38.4	39.8	43.3	28.28
	RMSEU	24.6	3.2	25.4	9.6	19.4	22	20.7	16.3	21.9	33.2	31.9	21.4	20.80
	RMSES	27.3	11.6	25.3	10.9	9.1	–	18.2	11.9	13.1	19.3	23.7	37.7	18.92
	NSE	0.29	0.6	0.28	0.77	0.62	0.53	0.57	0.53	0.03	0.01	0.06	0.34	0.39
GBAF	CC	0.78	0.75	0.53	–	0.88	0.66	0.58	0.73	0.67	0.35	0.35	0.58	0.62
	Ratio	0.8	0.85	0.58	–	0.91	0.79	0.57	0.87	0.64	1.42	0.63	0.46	0.77
	Bias	3.48	18.25	3.53	–	-1.55	-7.95	-12.51	14.08	1.96	-10.02	-25.08	-31.66	-4.32
	RMSE	22.5	21.8	35.9	–	16.3	26.2	37.1	24.2	21.8	33.7	43.1	53.8	30.58
	RMSEU	17.8	10	20.8	–	14.7	19.4	20	16.7	13.8	30.2	21.2	20	18.60
	RMSES	13.8	19.4	29.3	–	–	17.7	31.2	17.5	16.9	15.1	37.5	50	24.84
	NSE	0.6	0.49	0.27	–	0.77	0.37	0.25	0.26	0.44	-1.21	-0.46	-0.03	0.16
AVHRR	CC	0.8	–	0.8	–	0.76	0.68	0.58	0.79	0.69	0.32	0.7	0.79	0.69
	Ratio	0.91	–	0.87	–	0.87	1.15	0.83	0.9	0.89	0.3	0.95	0.43	0.81
	Bias	-1.15	–	5.96	–	5.24	-2.73	-7.04	0.16	-2.41	-47.83	-0.42	-25.32	-7.55
	RMSE	23.6	–	26.1	–	23.3	31	36	18.8	22.1	54.7	33.2	46.6	31.54
	RMSEU	21.2	–	22	–	19.5	29.8	27.9	16.6	18.8	–	29.8	14.6	22.24
	RMSES	10.4	–	14.1	–	12.7	8.4	22.7	8.7	11.6	54.2	14.6	44.2	20.16
	NSE	0.63	–	0.61	–	0.54	0.23	0.24	0.62	0.43	-2.79	0.42	0.29	0.12
MOD16	CC	0.57	0.94	0.71	0.95	0.82	0.74	0.71	0.81	0.67	0.53	0.59	0.65	0.72
	Ratio	0.64	1.26	0.77	0.8	1.11	0.81	0.74	1.09	0.66	1	1	0.46	0.86
	Bias	-7.88	-14.03	5.79	-4.07	-7.17	-4.51	-5.05	4.09	-6.41	-16.01	-23.76	-21.07	-8.34
	RMSE	36.9	16.7	30.7	11.1	23.4	24.3	29.6	19.4	20.4	40.4	44.3	47.2	28.70
	RMSEU	23	8.4	23	7.4	22	19.3	21.7	18.7	12.8	32.4	33.3	18.8	20.07
	RMSES	28.8	14.4	20.3	8.2	7.8	14.9	20.2	5.2	15.9	24.2	29.1	43.3	19.36
	NSE	0.28	0.24	0.48	0.87	0.55	0.52	0.5	0.57	0.39	0.12	0.14	0.23	0.41
PML	CC	0.68	0.99	0.68	0.93	0.8	0.81	0.68	0.77	0.7	0.57	0.61	0.82	0.75
	Ratio	0.8	1.04	0.81	1.22	0.98	0.97	0.79	0.96	1.01	0.94	0.83	0.56	0.91
	Bias	-6.6	-3	-3.39	0.47	-1.42	-6.07	-6.66	-0.59	6.48	-0.18	-16.04	-22.1	-4.93
	RMSE	33.2	4.1	31.5	13.3	21.9	22.2	31.7	19.8	21.1	34.5	37.5	40.5	25.94
	RMSEU	25.6	2.8	25.1	12.7	20.5	20.1	24.1	18.2	18.6	29.5	27.1	17.3	20.13
	RMSES	21.1	3.1	19	3.9	7.8	9.6	20.6	7.7	9.9	17.8	26	36.6	15.26
	NSE	0.42	0.95	0.44	0.79	0.61	0.6	0.43	0.55	0.33	0.19	0.16	0.43	0.49

504

505 Figure 8 illustrates the spatial distribution of multi-year average monthly precipitation data sourced
 506 from the Global Precipitation Climatology Centre (GPCC) and the calculated evapotranspiration (ET) by
 507 various models, namely WISEA, GLEAM, GBAF, AVHRR, MOD16, and PML. Comparing these
 508 precipitation and ET products may seem incompatible; nevertheless, this section focuses on the
 509 distribution patterns of rainfall and ET rather than on their specific values.

510



511

512 **Figure 8.** The spatial distribution of the multi-year average (2001-2019) for (a) GPCC (2001-2019), (b)
513 VISEA (2001-2020), (c) GLEAM (2003-2019), (d) GBAF (2001-2008), (e) AVHRR (2001-2006), (f)
514 MOD16 (2001-2014) and (g) PML (2003-2018).

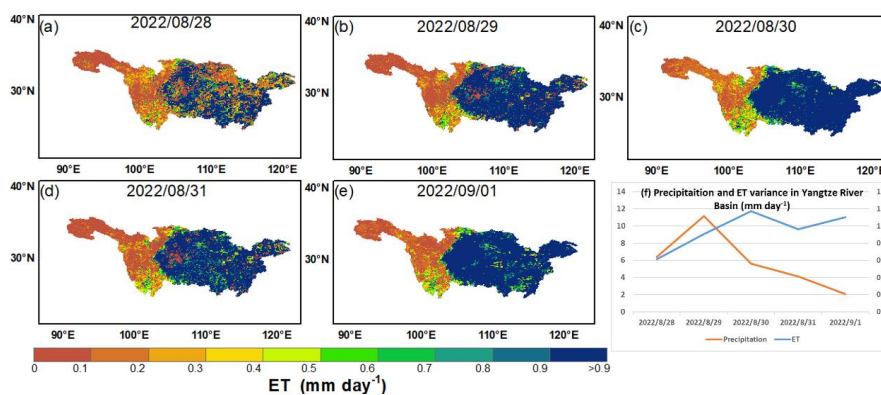
515 All six of these ET products exhibit similar and coherent spatial ET distributions, which align with
516 the precipitation distribution data from GPCC. The highest ET values (1,400 to 1,600 mm year⁻¹) are
517 predominantly concentrated in equatorial low-latitude regions with the highest precipitation levels (1,600
518 to 1,800 mm year⁻¹). These regions include South America (Amazon Basin), Central Africa (Congo
519 Basin), and Southeast Asia (encompassing Indonesia, Malaysia, parts of Thailand, and the Philippines),
520 which are known for their tropical rainforest climates. These ET estimates align with the findings of
521 Tapiador et al. (2012) and Panagos et al. (Panagos et al., 2017), who reported that the multi-year average
522 annual precipitation is approximately 2,000 mm year⁻¹.

523 Conversely, areas categorized as barren land (BAR), including deserts such as Sahara, Arabian,
524 Gobi, Kalahari, and large portions of Australia, as well as snow and ice (SI) areas like most parts of
525 Canada, Russia, and the Qinghai-Tibet Plateau in China, where the growing seasons are short, typically
526 falling below 400 mm year⁻¹. These areas are also characterized by the lowest annual precipitation,
527 ranging from 200 to 400 mm year⁻¹ according to GPCC precipitation data mm year⁻¹. ET estimates for
528 other land cover types fall within this range, varying from 400 to 1,400 mm year⁻¹, in close alignment
529 with the GPCC precipitation data, which falls between 600 to 1,600 mm year⁻¹.

530 Figure 9 presents the daily variations in ET from August 28th, 2022, to September 1st, 2022, within
531 the Yangtze River Basin, along with the mean ET and Global Unified Gauge-Based Analysis of Daily
532 Precipitation recorded during this period. According to a study by Zhang et al. (2023), the summer of
533 2022 witnessed a severe drought within the Yangtze River Basin. This drought commenced in July,
534 gradually relenting in late August and early September. Figure 9 visually represents the drought severity,



535 highlighting extremely low ET levels (below 0.2 mm day^{-1}) across most of the basin on August 28th,
536 2022. Subsequently, on August 29th, 2022, an upsurge in precipitation resulted in a corresponding
537 increase in ET (exceeding 0.8 mm day^{-1}) throughout the majority of the basin, as depicted in subfigures
538 (b)-(e).



539

540 **Figure 9.** Daily ET distribution of VISEA from August 28th to September 1st in 2022) (a)-(e) and mean
541 ET and Precipitation Variance in the Yangtze River Basin (f) during the same period.

542 In subfigure (f), the variances in mean ET and precipitation across the river basin during this period
543 are showcased. Notably, a substantial increase in rainfall (11 mm day^{-1}) on August 29th, 2022, was
544 responsible for the surge in ET (1.1 mm day^{-1}) on August 30th, 2022, indicating an alleviation of drought
545 conditions within the region. The consistent alignment of ET and precipitation variances underlines
546 VISEA's ability to capture near-real-time fluctuations in ET, particularly during drought events.

547 5. Discussion

548 While global ET products require at least 2 weeks to generate global actual ET measurement, we
549 developed VISEA, a satellite-based algorithm which is capable of generating near-real-time
550 evapotranspiration on a daily time step with a resolution of 0.05° . This algorithm is based Nishida et al.
551 (2003) satellite-based evaporation fraction algorithm. To assess its accuracy, we compared the calculated
552 ET with data from 149 flux towers around the world in various land use types.

553 Scale mismatch is a problem for many satellite-based ET products. The footprints of these flux towers
554 typically range from 100 to 200 meters, while the VISEA model outputs gridded cells at a resolution of
555 $0.05^\circ \times 0.05^\circ$ (nearly 25 km^2). This discrepancy introduces errors, especially since flux towers require a
556 uniform fetch, which may not represent the larger gridded cell. To enhance the validity of our
557 assessments, we assessed monthly values and spatial patterns of our ET measurements with five other
558 satellite-based ET products named MOD16, AVHRR, GLEAM, GBAF and PML (Figure 7 and 8).

559 The evapotranspiration is calculated with VISEA using shortwave downwards radiation, and
560 intermediate variables including daily air temperature and net radiation. The calculated
561 evapotranspiration generally matches local measurements and other model calculated values well but we



562 found significant biases (Figures 6 and 7). These biases largely arise from inaccuracies in the input ERA5-
563 Land shortwave radiation (Figure 3), improper application of the VI-Ts method (Figure 4), and
564 uncertainties in daily net radiation (Figure 5). Below we detail the origin of the biases.

565 Incoming shortwave radiation from ERA5-Land is employed to derive the available energy for
566 vegetation coverage and bare soil (Eq. 20 and 21), which are the main parameters for calculating daily
567 ET (Eq. 22). While ERA5-Land is widely utilized as a reanalysis dataset, offering near-real-time land
568 variables by integrating model data with global observations based on physical laws. However, the
569 accuracy of shortwave radiation from ERA5-Land seems compromised in savannas (Figure 3) due to the
570 challenges associated with simulating radiation transmission under land-use changes and aerosol
571 pollution from natural or anthropogenic sources.

572 Air temperature is an important parameter in determining the daily evaporation fraction of bare soil
573 (Eq. 14), canopy surface resistance (Eq. A1), aerodynamic resistance of the bare soil (Eq. A9),
574 atmospheric emissivity (B1), available energy for vegetation coverage and bare soil (Eq. 20 and 21).
575 Since air temperature is not measured directly by satellites, many other ET product use therefore ground
576 observations, land model or reanalysis data. In contrast, VISEA derives the air temperature from the
577 negative linear relationship between vegetation index (VI) and surface temperature (Ts) using the VI-Ts
578 method (section 2.1.3). It gives very good results under grass land, open shrubland and woody savannas
579 landcover types, as shown in Figure 4. However, in regions where the vegetation index and temperature
580 data in adjacent grid cells show small variations, such as dense forests and bare lands and deserts. Also,
581 in regions with freezing temperatures, the VI-Ts method does perform well, because warmer temperature
582 is related to increased vegetation, opposite the other regions, where there is a negative.

583 Another source of bias stems from our VISEA model, is the daily net radiation's uncertainties. which
584 are primarily attributed to the input shortwave radiation and air temperature, as indicated by the energy
585 budget equation (Eq. 17).

586 The ET calculation in VISEA relies solely on vegetation coverage as an indirect constraint and does
587 not explicitly account for water availability. This approach overestimates evapotranspiration (ET) in
588 regions with excessively high available energy. Additionally, VISEA tends to underestimate ET in colder
589 areas, such as the western regions of Canada, which is attributed to the model's failure to account for
590 evaporation from frozen surfaces in its ET calculations.

591 In our efforts to enhance the model, we are planning to refine the model's treatment of frozen surfaces
592 and bare lands, aiming to improve accuracy in colder and arid regions. Future works include
593 improvements that need to be made to reduce the bias in ET, refine the VI-TS method, explore additional
594 factors like aerosols and land use changes, and enhance spatial resolution.

595 **6. Conclusion**

596 In recent decades, several ET products using satellites have been developed, but few of them
597 provide near-real-time global terrestrial ET estimates. Despite being updated at the fastest rate, the



598 MOD16 ET dataset still encounters a delay of more than two weeks. In this study, we provide a satellite-
599 based near-real-time global daily terrestrial ET estimates by incorporating near-real-time updated hourly
600 shortwave radiation data from ERA5 and MODIS land products at a spatial resolution of 0.05°. The
601 assessments indicate that near-real-time ET estimation with VISEA achieves comparable accuracy to
602 other existing data products and offers a significantly shorter time frame for daily data availability.

603 The new VISEA aligns well with measurements at 149 tower flux sites distributed globally in both
604 daily and monthly time scales. It exhibits superior accuracy compared to the other five ET products for
605 DNF land cover types and competitive accuracy for most land cover types. However, like the other five
606 ET products, it encounters greater uncertainties for the SAV land cover type. In the comparison of the
607 multiple-year average spatial distribution of other monthly ET products and GPCC precipitation, VISEA
608 aligns with GPCC and other ET estimates in most areas worldwide, indicating its adherence to the water
609 balance in those regions. However, VISEA exhibits slightly higher estimates in the Sahara region and
610 lower estimations in the western Canada. In future studies, the VISA ET algorithm can be enhanced by
611 incorporating more precise models for the radiation estimation in savanna and the evaporation from the
612 frozen surface. These improvements will greatly contribute to enhancing the overall accuracy of the
613 algorithm. The satellite-based near-real-time global daily terrestrial ET estimates could be beneficial for
614 meteorology and hydrology applications requiring real-time data, especially in coordinating relief efforts
615 during droughts.

616 **7. Code Availability**

617 Python code to synthesise the results and to generate the figures of VISEA results and the codes for
618 generating the global ET products can be obtained through the public repository at
619 <https://doi.org/10.6084/m9.figshare.24647721.v1> (Huang, 2023c).

620 **8. Data Availability**

621 The VISEA ET data can be obtained from <https://data.tpd.c.cn/en/data/236e33bf-e66b-4682-bbc1-274de1dcbcd3> (Huang, 2023a).

623 **8.1 Input data**

624 MOD11C1 can be obtained at <https://e4ftl01.cr.usgs.gov/MOLT/MOD11C1.061/>. MOD09CMG can be
625 obtained at <https://e4ftl01.cr.usgs.gov/MOLT/MOD09CMG.061/>. MCD43C3 can be obtained at
626 <https://e4ftl01.cr.usgs.gov/MOTA/MCD43C3.061/>. MOD13C1 can be obtained at
627 <https://e4ftl01.cr.usgs.gov/MOLT/MOD13C1.061/>. MCD12C1 can be obtained at
628 <https://e4ftl01.cr.usgs.gov/MOLT/MOD21C1.061/>. ERA5-Land shortwave radiation data can be
629 obtained at <https://cds.climate.copernicus.eu/cdsapp#!/dataset/reanalysis-era5-land?tab=form>.

630 **8.2 Evaluation data**



631 FLUXNET2015 flux towers data (FLUXNET2015: CC-BY-4.0 33) can be obtained at
632 <https://fluxnet.org/data/download-data/>. The GLEAM ET dataset was obtained from
633 <https://www.gleam.eu/#downloads> (an email is required to receive a password for the SFTP). The GBAF
634 ET dataset was acquired from <https://www.bgc-jena.mpg.de/geodb/projects/Data.php>. MOD16 ET was
635 obtained from
636 http://files.ntsug.umd.edu/data/NTSG_Products/MOD16/MOD16A2_MONTHLY.MERRA_GMAO_1k
637 [mALB/Previous/](http://files.ntsug.umd.edu/data/ET_global_monthly_ORIG/Global_1DegResolution/ASCIIFormat/). Additionally, the AVHRR ET dataset was sourced from
638 http://files.ntsug.umd.edu/data/ET_global_monthly_ORIG/Global_1DegResolution/ASCIIFormat/.
639 Lastly, the PML ET dataset was obtained from [https://www.tpdac.ac.cn/zh-hans/data/48c16a8d-d307-](https://www.tpdac.ac.cn/zh-hans/data/48c16a8d-d307-4973-abab-972e9449627c)
640 [4973-abab-972e9449627c](https://www.tpdac.ac.cn/zh-hans/data/48c16a8d-d307-4973-abab-972e9449627c).

641 The precipitation from Global Precipitation Climatology Centre (GPCC) data was as obtained at
642 [https://cds.climate.copernicus.eu/cdsapp#!/dataset/insitu-gridded-observations-global-and-](https://cds.climate.copernicus.eu/cdsapp#!/dataset/insitu-gridded-observations-global-and-regional?tab=form)
643 [regional?tab=form](https://cds.climate.copernicus.eu/cdsapp#!/dataset/insitu-gridded-observations-global-and-regional?tab=form). The precipitation from Global Unified Gauge-Based Analysis of Daily Precipitation
644 (CPC) was obtained at https://downloads.psl.noaa.gov/Datasets/cpc_global_precip/precip.2022.nc

645 Other data that supports the analysis and conclusions of this work is available at
646 https://figshare.com/articles/dataset/Satellite-based_Near-Real
647 [Time_Global_Daily_Terrestrial_Evapotranspiration_Estimates/24669306](https://figshare.com/articles/dataset/Satellite-based_Near-Real) (Huang, 2023d).

648



649 **Appendix**

650 **Appendix A. Determining the resistances of vegetation canopy and bare soil surface**

651 The canopy surface resistance of the vegetation, denoted as $r_{c\,veg}$ ($s\,m^{-1}$), was determined using the
652 relationship established by Jarvis et al. (1976), is equivalent to:

653
$$\frac{1}{r_{c\,veg}} = \frac{f_1(T_a)f_2(PAR)f_3(VPD)f_4(\varphi)f_5(CO_2)}{r_{c\,MIN}} + \frac{1}{r_{cuticle}} \quad (A1)$$

654 The minimum resistance $r_{c\,MIN}$ ($s\,m^{-1}$) is defined as 33 ($s\,m^{-1}$) for cropland and 50 ($s\,m^{-1}$) for forest
655 as determined by Tang et al. (2009); the canopy resistance related to diffusion through the cuticle layer
656 of leaves $r_{cuticle}$ is set at 100,000 ($s\,m^{-1}$) in the Biome-BGC model is according to White et al. (2000).
657 The relationships involving air temperature T_a , $f_1(T_a)$ and photosynthetic active radiation PAR , $f_2(PAR)$
658 expressed by the functions provided Jarvis et al. (1976):

659
$$f_1(T_a) = \left(\frac{T_a - T_n}{T_o - T_n}\right) \left(\frac{T_x - T_a}{T_x - T_a}\right)^{\left(\frac{T_x - T_o}{T_o - T_n}\right)} \quad (A2)$$

660 The minimum, optimal, and maximum temperatures for stomatal activity are denoted as T_n , T_o and
661 T_x , respectively. As per Tang et al. (2009), T_n is set to 275.85 K, T_o to 304.25 K, and T_x to 318.45 K. The
662 expression for the function $f_2(PAR)$ is provided below:
663

664
$$f_2(PAR) = \frac{PAR}{PAR + A} \quad (A3)$$

665 where PAR is photosynthetic active radiation per unit area and time ($\mu\,mol\,m^{-2}\,s^{-1}$) calculated by
666 incoming solar radiation multiplied by 2.05 (White et al., 2000); A is a parameter related to photon
667 absorption efficiency at low light intensity, which was set to 152 $\mu\,mol\,m^{-2}\,s^{-1}$ 20; Nishida³² found that
668 in Eq. A1 the following functions can be omitted without great loss of accuracy: the functions depending
669 on vapor pressure deficit, $f_3(VPD)$, leaf water potential $f_4(\varphi)$ and carbon dioxide vapor pressure,
670 $f_5(CO_2)$.

671 The photosynthetic active radiation per unit area and time (PAR), measured in $\mu\,mol\,m^{-2}\,s^{-1}$, is
672 computed by multiplying incoming solar radiation by 2.05, as outlined by White et al. (2000). The
673 parameter A , associated with photon absorption efficiency at low light intensity, is established at 152 $\mu\,mol\,m^{-2}\,s^{-1}$.
674 Nishida et al. (2003) observed that, in Eq. A1, the functions tied to vapor pressure deficit
675 $f_3(VPD)$, leaf water potential $f_4(\varphi)$, and carbon dioxide vapor pressure $f_5(CO_2)$ can be omitted without
676 significant loss of accuracy.

677 The aerodynamic resistance of the canopy, denoted as $r_{a\,veg}$ ($s\,m^{-1}$), is computed for forest cover,
678 grassland, and cropland using the empirical formulae presented by Nishida et al. (2003) for both
679 instantaneous and daily values.



$$680 \quad \frac{1}{r_{a \text{ veg}}(\text{forest})} = 0.008 U_{50m} \quad (A4)$$

681 The wind speed at a height of 50 meters above the canopy (U_{50m}) is used to determine the
 682 aerodynamic resistance for grassland and cropland, as follows:

$$683 \quad \frac{1}{r_{a \text{ veg}}(\text{grassland \& cropland})} = 0.003 U_{1m} \quad (A5)$$

684 where U_{1m} is the wind speed 1m above the canopy (m s^{-1}). The wind speed as a function of the
 685 height z , $U(z)$ can be calculated by the logarithm profile of wind. A recent study found that the velocity
 686 log law does not apply to a stratified atmospheric boundary layer (Cheng et al., 2011). Thus A4 and A5
 687 are valid under neutral boundary layer conditions. Since $r_{a \text{ veg}}$ is calculated differently for forests (Eq.
 688 A4) and grasslands/croplands (Eq. A5), we used the land cover classes from the yearly International
 689 Geosphere-Biosphere Programme (IGBP) (MCD12C1) to identify the land cover and choice the different
 690 equation of $r_{a \text{ veg}}$. U_{50m} and U_{1m} were calculated by the logarithm profile of wind:

$$691 \quad U(z) = U_{\text{shear}} \ln \left[\frac{(z-d)}{z_0} \right] / k \quad (A6)$$

692 where U_{shear} is the shear velocity (m s^{-1}); z is the height (m); d is the surface displacement (m); z_0
 693 is the roughness length, we followed Nishida et al. (2003), set as 0.005 m for bare soil and 0.01 m for
 694 grassland; k is the von Kármán's constant and set as 0.4 following Nishida (Nishida et al., 2003). The
 695 shear velocity U_{shear} was calculated as:

$$696 \quad U_{\text{shear}} = U_{1m \text{ soil}} \frac{0.4}{\ln \left(\frac{1}{0.005} \right)} \quad (A7)$$

697 where the $U_{1m \text{ soil}}$ is the wind speed of bare soil at 1 m height (m s^{-1}), it was calculated as:

$$698 \quad U_{1m \text{ soil}} = 1/0.0015 r_{a \text{ soil}} \quad (A8)$$

699 The Vegetation Index-surface Temperature (VI-T_s) diagram (Nishida et al., 2003) can be utilized to
 700 compute the instantaneous air temperature. This is achieved by utilizing MODIS instantaneous surface
 701 temperature/emissivity data (MOD11C1) and daily-calculated NDVI as input parameters.

702 The aerodynamic resistance of the bare soil, denoted as $r_{a \text{ soil}}$ (s m^{-1}), was determined by Nishida
 703 et al. (2003). This calculation assumes that the maximum surface temperature of bare soil $T_{\text{soil max}}$ (K)
 704 happens when the sum of latent heat flux and sensible heat flux of the bare soil, referred to as the available
 705 energy of bare soil Q_{soil} (W m^{-2}), is utilized as the sensible heat flux, while the latent heat flux is set to
 706 zero.

$$707 \quad r_{a \text{ soil}} = \frac{\rho C_p (T_{\text{soil max}} - T_a)}{Q_{\text{soil}}} \quad (A9)$$

708 $r_{a \text{ soil}}$ is the aerodynamic resistance of the bare soil, (s m^{-1}), ρ is the air density, kg m^{-3} ; C_p is the
 709 specific heat of the air, ($\text{J kg}^{-1} \text{K}^{-1}$); T_a is the air temperature (K), Q_{soil} is the available energy of bare soil
 710 (W m^{-2}).



711 To compute the canopy surface resistance of bare soil, denoted as $r_{c\ soil}$ ($s\ m^{-1}$), we adhere to the
712 methodologies outlined in the works of Griend and Owe (1994) and Mu et al. (2007):

713
$$r_{c\ soil} = r_{tot} - r_{a\ soil} \quad (A10)$$

714
$$r_{tot} = \frac{1.0}{\left(\frac{r_a}{293.15}\right)^{1.75} \frac{101300}{P}} * 107.0 \quad (A11)$$

715 The total aerodynamic resistance r_{tot} ($s\ m^{-1}$) is composed of the aerodynamic resistance over the
716 bare soil $r_{a\ soil}$ ($s\ m^{-1}$), with atmospheric pressure P set at 101,300 Pa.

717



718 **Appendix B. The calculation of atmospheric emissivity for clear sky**

719 As per Brutsaert (1975), the atmospheric emissivity ε_a^d for clear sky under standard humidity and
720 temperature conditions is

$$721 \quad \varepsilon_a^d = 1.24 \times (e_a^d / T_a^d)^{1/7} \quad (B1)$$

722 where e_a^d represents the daily water vapor pressure (kPa). To calculate e_a^d , it is necessary to
723 compute the slope of the saturated vapor (Δ) as:

$$724 \quad \Delta = \frac{4098 \left[0.6108 \exp \left[\frac{17.27 T_a}{T_a + 237.3} \right] \right]}{(T_a + 237.3)^2} \quad (B2)$$

725 VPD is the vapor pressure deficit of the air (kPa), which is expressed as:

$$726 \quad \text{VPD} = e^0(T_a) - e_a \quad (B3)$$

$$727 \quad e^0(T_a) = 0.6108 \exp \left[\frac{17.27 T_a}{T_a + 237.3} \right] \quad (B4)$$

$$728 \quad e_a = e^0(T_{dew}) \quad (B5)$$

$$729 \quad e^0(T_{dew}) = 0.6108 \exp \left[\frac{17.27 T_{dew}}{T_{dew} + 237.3} \right] \quad (B6)$$

730 The expression within parentheses denotes the independent variable, where, $e^0(T_a)$ represents the
731 saturation vapor pressure (kPa) at the air temperature T_a (°C); e_a is the actual vapor pressure (kPa);
732 $e^0(T_{dew})$ is the saturation vapor pressure (kPa) at the dew point temperature T_{dew} (°C). For forest, water
733 surface, and cropland T_{dew} is set to the minimum air temperature during the day. In arid regions such as
734 bare soil and non-irrigated grassland, T_{dew} may be 2-3 °C lower than T_{min} . Therefore, 2 °C is subtracted
735 is subtracted from T_{min} in arid and semiarid areas to derive T_{dew} . While these simplifications might
736 introduce a bias in the final calculated ET value, our initial results indicate that the effect is negligible.

737 **Acknowledgements**

738 This study is supported by the National Key Research and Development Program of China
739 (No.2017YFA0603703). We employed ChatGPT3.5 to enhance the quality of our English writing and
740 grammar.

741 **Author contributions**

742 L. H. had the original idea and drafted the paper with help from Y. L.; J. M. C. Q. T., T. S., W. C. and
743 W. S. participated in the discussion and the many manuscript revisions.

744 **Competing interests**

745 The authors declare no competing interests.



746 References

- 747 Aschonitis, V., Touloumidis, D., ten Veldhuis, M.-C., and Coenders-Gerrits, M.: Correcting
748 Thornthwaite potential evapotranspiration using a global grid of local coefficients to support
749 temperature-based estimations of reference evapotranspiration and aridity indices, *Earth System
750 Science Data*, 14, 163–177, <https://doi.org/10.5194/essd-14-163-2022>, 2022.
- 751 Awada, H., Di Prima, S., Sirca, C., Giadrossich, F., Marras, S., Spano, D., and Pirastru, M.: A remote
752 sensing and modeling integrated approach for constructing continuous time series of daily actual
753 evapotranspiration, *Agricultural Water Management*, 260, 107320,
754 <https://doi.org/10.1016/j.agwat.2021.107320>, 2022.
- 755 Barrios, J. M., Ghilain, N., Arboleda, A., and Gellens-Meulenberghs, F.: Retrieving daily
756 evapotranspiration from the combination of geostationary and polar-orbit satellite data, in: 2015 8th
757 International Workshop on the Analysis of Multitemporal Remote Sensing Images (Multi-Temp),
758 2015 8th International Workshop on the Analysis of Multitemporal Remote Sensing Images (Multi-
759 Temp), 1–4, <https://doi.org/10.1109/Multi-Temp.2015.7245797>, 2015.
- 760 Becker, A., Finger, P., Meyer-Christoffer, A., Rudolf, B., Schamm, K., Schneider, U., and Ziese, M.:
761 A description of the global land-surface precipitation data products of the Global Precipitation
762 Climatology Centre with sample applications including centennial (trend) analysis from 1901–
763 present, *Earth System Science Data*, 5, 71–99, <https://doi.org/10.5194/essd-5-71-2013>, 2013.
- 764 Brutsaert, W.: On a derivable formula for longwave radiation from clear skies, *Water Resources
765 Research*, 11, 742–744, <https://doi.org/10.1029/WR011i005p00742>, 1975.
- 766 Chang, K. and Zhang, Q.: Modeling of downward longwave radiation and radiative cooling potential
767 in China, *Journal of Renewable and Sustainable Energy*, 11, 066501,
768 <https://doi.org/10.1063/1.5117319>, 2019.
- 769 Cheng, L., Xu, Z., Wang, D., and Cai, X.: Assessing interannual variability of evapotranspiration at
770 the catchment scale using satellite-based evapotranspiration data sets, *Water Resources Research*,
771 47, <https://doi.org/10.1029/2011WR010636>, 2011.
- 772 Copernicus Climate Change Service: Crop productivity and evapotranspiration indicators from 2000
773 to present derived from satellite observations, <https://doi.org/10.24381/CDS.B2F6F9F6>, 2020.
- 774 De Bruin, H. a. R.: A Model for the Priestley-Taylor Parameter α , *J. Climate Appl. Meteor.*, 22, 572–
775 578, [https://doi.org/10.1175/1520-0450\(1983\)022<0572:AMFTPT>2.0.CO;2](https://doi.org/10.1175/1520-0450(1983)022<0572:AMFTPT>2.0.CO;2), 1983.
- 776 Didan, K.: MOD13C1 MODIS/Terra Vegetation Indices 16-Day L3 Global 0.05Deg CMG V006
777 [data set], <https://doi.org/10.5067/MODIS/MOD13C1.006>, n.d.
- 778 Fisher, J. B., Lee, B., Purdy, A. J., Halverson, G. H., Dohlen, M. B., Cawse-Nicholson, K., Wang,
779 A., Anderson, R. G., Aragon, B., Arain, M. A., Baldocchi, D. D., Baker, J. M., Barral, H., Bernacchi,
780 C. J., Bernhofer, C., Biraud, S. C., Bohrer, G., Brunzell, N., Cappelaere, B., Castro-Contreras, S.,
781 Chun, J., Conrad, B. J., Cremonese, E., Demarty, J., Desai, A. R., De Ligne, A., Foltýnová, L.,
782 Goulden, M. L., Griffis, T. J., Grünwald, T., Johnson, M. S., Kang, M., Kelbe, D., Kowalska, N.,
783 Lim, J.-H., Maïnassara, I., McCabe, M. F., Missik, J. E. C., Mohanty, B. P., Moore, C. E., Morillas,
784 L., Morrison, R., Munger, J. W., Posse, G., Richardson, A. D., Russell, E. S., Ryu, Y., Sanchez-
785 Azofeifa, A., Schmidt, M., Schwartz, E., Sharp, I., Šigut, L., Tang, Y., Hulley, G., Anderson, M.,
786 Hain, C., French, A., Wood, E., and Hook, S.: ECOSTRESS: NASA’s Next Generation Mission to
787 Measure Evapotranspiration From the International Space Station, *Water Resources Research*, 56,
788 e2019WR026058, <https://doi.org/10.1029/2019WR026058>, 2020.
- 789 Friedl, M., D. Sulla-Menashe.: MCD12C1 MODIS/Terra+Aqua Land Cover Type Yearly L3 Global
790 0.05Deg CMG V006 [data set], <https://doi.org/10.5067/MODIS/MCD12C1.006>, 2015.



- 791 Goforth, M. A., Gilchrist, G. W., and Sirianni, J. D.: Cloud effects on thermal downwelling sky
792 radiance, in: *Thermosense XXIV*, 203–213, <https://doi.org/10.1117/12.459570>, 2002.
- 793 Griend, A. A. van de and Owe, M.: Bare soil surface resistance to evaporation by vapor diffusion
794 under semiarid conditions, *Water Resources Research*, 30, 181–188,
795 <https://doi.org/10.1029/93WR02747>, 1994.
- 796 Han, C., Ma, Y., Wang, B., Zhong, L., Ma, W., Chen, X., and Su, Z.: Long-term variations in actual
797 evapotranspiration over the Tibetan Plateau, *Earth System Science Data*, 13, 3513–3524,
798 <https://doi.org/10.5194/essd-13-3513-2021>, 2021.
- 799 He, S., Zhang, Y., Ma, N., Tian, J., Kong, D., and Liu, C.: A daily and 500&thinspm coupled
800 evapotranspiration and gross primary production product across China during 2000–2020, *Earth
801 System Science Data*, 14, 5463–5488, <https://doi.org/10.5194/essd-14-5463-2022>, 2022.
- 802 Huang, L.: Satellite-based Near-Real-Time Global Terrestrial Evapotranspiration Estimation
803 National Tibetan Plateau / Third Pole Environment Data Center [data set],
804 <https://doi.org/10.11888/Terre.tpd.c.300782>. <https://cstr.cn/18406.11.Terre.tpd.c.300782>, 2023a.
- 805 Huang, L., Luo, Y., Steenhuis, T., Tang, Q., Cheng, W., Shi, W., Xia, X., Zhao, D., and Liao, Z.: An
806 Improved Satellite-Based Evapotranspiration Procedure for China, *Earth and Space Science*, 10,
807 e2023EA002949, <https://doi.org/10.1029/2023EA002949>, 2023b.
- 808 Huang, L.: Satellite-based Near-Real-Time Global Daily Terrestrial Evapotranspiration Estimates.
809 figshare. [Software]. <https://doi.org/10.6084/m9.figshare.24647721.v1,2023c>.
- 810 Huang, L.: Satellite-based Near-Real-Time Global Daily Terrestrial Evapotranspiration Estimates.
811 figshare [data set], <https://doi.org/10.6084/m9.figshare.24669306.v1,2023d>.
- 812 Huang, L., Li, Z., Tang, Q., Zhang, X., Liu, X., and Cui, H.: Evaluation of satellite-based
813 evapotranspiration estimates in China, *JARS*, 11, 026019, <https://doi.org/10.1117/1.JRS.11.026019>,
814 2017.
- 815 Huang, L., Steenhuis, T. S., Luo, Y., Tang, Q., Tang, R., Zheng, J., Shi, W., and Qiao, C.: Revisiting
816 Daily MODIS Evapotranspiration Algorithm Using Flux Tower Measurements in China, *Earth and
817 Space Science*, 8, e2021EA001818, <https://doi.org/10.1029/2021EA001818>, 2021.
- 818 Idso, S. B., Aase, J. K., and Jackson, R. D.: Net radiation — soil heat flux relations as influenced by
819 soil water content variations, *Boundary-Layer Meteorol*, 9, 113–122,
820 <https://doi.org/10.1007/BF00232257>, 1975.
- 821 Jarvis, P. G., Monteith, J. L., and Weatherley, P. E.: The interpretation of the variations in leaf water
822 potential and stomatal conductance found in canopies in the field, *Philosophical Transactions of the
823 Royal Society of London. B, Biological Sciences*, 273, 593–610,
824 <https://doi.org/10.1098/rstb.1976.0035>, 1976.
- 825 Jiang, H., Yang, Y., Bai, Y., and Wang, H.: Evaluation of the Total, Direct, and Diffuse Solar
826 Radiations From the ERA5 Reanalysis Data in China, *IEEE Geoscience and Remote Sensing Letters*,
827 17, 47–51, <https://doi.org/10.1109/LGRS.2019.2916410>, 2020.
- 828 Jung, M.: FLUXCOM Global Land Energy Fluxes, [data set],
829 https://doi.org/10.17871/FLUXCOM_EnergyFluxes_v1,2018.
- 830 Jung, M., Reichstein, M., and Bondeau, A.: Towards global empirical upscaling of FLUXNET eddy
831 covariance observations: validation of a model tree ensemble approach using a biosphere model,
832 *Biogeosciences*, 6, 2001–2013, <https://doi.org/10.5194/bg-6-2001-2009>, 2009.
- 833 Jung, M., Reichstein, M., Ciais, P., Seneviratne, S. I., Sheffield, J., Goulden, M. L., Bonan, G.,



- 834 Cescatti, A., Chen, J., de Jeu, R., Dolman, A. J., Eugster, W., Gerten, D., Gianelle, D., Gobron, N.,
835 Heinke, J., Kimball, J., Law, B. E., Montagnani, L., Mu, Q., Mueller, B., Oleson, K., Papale, D.,
836 Richardson, A. D., Roupsard, O., Running, S., Tomelleri, E., Viovy, N., Weber, U., Williams, C.,
837 Wood, E., Zaehle, S., and Zhang, K.: Recent decline in the global land evapotranspiration trend due
838 to limited moisture supply, *Nature*, 467, 951–954, <https://doi.org/10.1038/nature09396>, 2010.
- 839 Jung, M., Koirala, S., Weber, U., Ichii, K., Gans, F., Camps-Valls, G., Papale, D., Schwalm, C.,
840 Tramontana, G., and Reichstein, M.: The FLUXCOM ensemble of global land-atmosphere energy
841 fluxes, *Sci Data*, 6, 1–14, <https://doi.org/10.1038/s41597-019-0076-8>, 2019.
- 842 Martens, B., Miralles, D. G., Lievens, H., van der Schalie, R., de Jeu, R. A. M., Fernández-Prieto,
843 D., Beck, H. E., Dorigo, W. A., and Verhoest, N. E. C.: GLEAM v3: satellite-based land evaporation
844 and root-zone soil moisture, *Geoscientific Model Development*, 10, 1903–1925,
845 <https://doi.org/10.5194/gmd-10-1903-2017>, 2017.
- 846 Martin Jung, Sujan Koirala, Ulrich Weber, Kazuhito Ichii, Fabian Gans, Gustau Camps-Valls, Dario
847 Papale, Christopher Schwalm, Gianluca tramontana & Markus Reichstein: FLUXCOM Global Land
848 Energy Fluxes, https://doi.org/10.17871/FLUXCOM_EnergyFluxes_v1, 2018.
- 849 Miralles, D. G., Holmes, T. R. H., De Jeu, R. a. M., Gash, J. H., Meesters, A. G. C. A., and Dolman,
850 A. J.: Global land-surface evaporation estimated from satellite-based observations, *Hydrology and
851 Earth System Sciences*, 15, 453–469, <https://doi.org/10.5194/hess-15-453-2011>, 2011.
- 852 Mu, Q., Heinsch, F. A., Zhao, M., and Running, S. W.: Development of a global evapotranspiration
853 algorithm based on MODIS and global meteorology data, *Remote Sensing of Environment*, 111,
854 519–536, <https://doi.org/10.1016/j.rse.2007.04.015>, 2007.
- 855 Mu, Q., Zhao, M., and Running, S. W.: Improvements to a MODIS global terrestrial
856 evapotranspiration algorithm, *Remote Sensing of Environment*, 115, 1781–1800,
857 <https://doi.org/10.1016/j.rse.2011.02.019>, 2011.
- 858 Muñoz Sabater, J.: ERA5-Land hourly data from 1950 to present., [https://doi.org/DOI:
859 10.24381/cds.e2161bac](https://doi.org/DOI:10.24381/cds.e2161bac), 2019.
- 860 Naud, C. M., Booth, J. F., and Genio, A. D. D.: Evaluation of ERA-Interim and MERRA Cloudiness
861 in the Southern Ocean, *Journal of Climate*, 27, 2109–2124, [https://doi.org/10.1175/JCLI-D-13-
00432.1](https://doi.org/10.1175/JCLI-D-13-
862 00432.1), 2014.
- 863 Nishida, K., Nemani, R. R., Running, S. W., and Glassy, J. M.: An operational remote sensing
864 algorithm of land surface evaporation, *Journal of Geophysical Research: Atmospheres*, 108,
865 <https://doi.org/10.1029/2002JD002062>, 2003.
- 866 Panagos, P., Borrelli, P., Meusburger, K., Yu, B., Klik, A., Yang, J., Ni, J., Chattopadhyay, N.,
867 Sadeghi, S. H., Hazbavi, Z., Zabihi, M., Larionov, G., Krasnov, S., Gorobets, A., Levi, Y., Erpul, G.,
868 Birkel, C., and Ballabio, C.: Global rainfall erosivity assessment based on high-temporal resolution
869 rainfall records, *Scientific Reports*, 7, <https://doi.org/10.1038/s41598-017-04282-8>, 2017.
- 870 Pastorello, G., Trotta, C., Canfora, E., Chu, H., Christianson, D., Cheah, Y.-W., Poindexter, C., Chen,
871 J., Elbashandy, A., Humphrey, M., Isaac, P., Polidori, D., Reichstein, M., Ribeca, A., van Ingen, C.,
872 Vuichard, N., Zhang, L., Amiro, B., Ammann, C., Arain, M. A., Ardö, J., Arkebauer, T., Arndt, S. K.,
873 Arriga, N., Aubinet, M., Aurela, M., Baldocchi, D., Barr, A., Beamesderfer, E., Marchesini, L. B.,
874 Bergeron, O., Beringer, J., Bernhofer, C., Berveiller, D., Billesbach, D., Black, T. A., Blanken, P. D.,
875 Bohrer, G., Boike, J., Bolstad, P. V., Bonal, D., Bonnefond, J.-M., Bowling, D. R., Bracho, R.,
876 Brodeur, J., Brümmer, C., Buchmann, N., Burban, B., Burns, S. P., Buysse, P., Cale, P., Cavagna,
877 M., Cellier, P., Chen, S., Chini, I., Christensen, T. R., Cleverly, J., Collalti, A., Consalvo, C., Cook,
878 B. D., Cook, D., Coursolle, C., Cremonese, E., Curtis, P. S., D’Andrea, E., da Rocha, H., Dai, X.,
879 Davis, K. J., Cinti, B. D., Grandcourt, A. de, Ligne, A. D., De Oliveira, R. C., Delpierre, N., Desai,
880 A. R., Di Bella, C. M., Tommasi, P. di, Dolman, H., Domingo, F., Dong, G., Dore, S., Duce, P.,



- 881 Dufrêne, E., Dunn, A., Dušek, J., Eamus, D., Eichelmann, U., ElKhidir, H. A. M., Eugster, W.,
882 Ewenz, C. M., Ewers, B., Famulari, D., Fares, S., Feigenwinter, I., Feitz, A., Fensholt, R., Filippa,
883 G., Fischer, M., Frank, J., Galvagno, M., et al.: The FLUXNET2015 dataset and the ONEFlux
884 processing pipeline for eddy covariance data, *Sci Data*, 7, 225, [https://doi.org/10.1038/s41597-020-](https://doi.org/10.1038/s41597-020-0534-3)
885 0534-3, 2020.
- 886 Pereira, A. R.: The Priestley–Taylor parameter and the decoupling factor for estimating reference
887 evapotranspiration, *Agricultural and Forest Meteorology*, 125, 305–313,
888 <https://doi.org/10.1016/j.agrformet.2004.04.002>, 2004.
- 889 Schaaf, C., Wang, Z.: MCD43C1 MODIS/Terra+Aqua BRDF/AlbedoModel Parameters Daily L3
890 Global 0.05Deg CMG V006 [data set], <https://doi.org/10.5067/MODIS/MCD43C1.006>, 2015.
- 891 Schneider, U., Becker, A., Finger, P., Meyer-Christoffer, A., Ziese, M., and Rudolf, B.: GPCP’s new
892 land surface precipitation climatology based on quality-controlled in situ data and its role in
893 quantifying the global water cycle, *Theor Appl Climatol*, 115, 15–40,
894 <https://doi.org/10.1007/s00704-013-0860-x>, 2014.
- 895 Schneider, U., Finger, P., Meyer-Christoffer, A., Rustemeier, E., Ziese, M., and Becker, A.:
896 Evaluating the Hydrological Cycle over Land Using the Newly-Corrected Precipitation Climatology
897 from the Global Precipitation Climatology Centre (GPCC), *Atmosphere*, 8, 52,
898 <https://doi.org/10.3390/atmos8030052>, 2017.
- 899 Software/model code: Huang, L.: Satellite-based Near-Real-Time Global Daily Terrestrial
900 Evapotranspiration Estimates, figshare [code], <https://doi.org/10.6084/m9.figshare.24647721.v1>,
901 2023.
- 902 Su, B., Huang, J., Mondal, S. K., Zhai, J., Wang, Y., Wen, S., Gao, M., Lv, Y., Jiang, S., Jiang, T.,
903 and Li, A.: Insight from CMIP6 SSP-RCP scenarios for future drought characteristics in China,
904 *Atmospheric Research*, 105375, <https://doi.org/10.1016/j.atmosres.2020.105375>, 2020.
- 905 Tang, Q., Peterson, S., Cuenca, R. H., Hagimoto, Y., and Lettenmaier, D. P.: Satellite-based near-
906 real-time estimation of irrigated crop water consumption, *Journal of Geophysical Research:*
907 *Atmospheres*, 114, <https://doi.org/10.1029/2008JD010854>, 2009.
- 908 Tang, R. and Li, Z.-L.: An improved constant evaporative fraction method for estimating daily
909 evapotranspiration from remotely sensed instantaneous observations, *Geophysical Research Letters*,
910 44, 2319–2326, <https://doi.org/10.1002/2017GL072621>, 2017.
- 911 Tang, R., Li, Z.-L., Sun, X., and Bi, Y.: Temporal upscaling of instantaneous evapotranspiration on
912 clear-sky days using the constant reference evaporative fraction method with fixed or variable
913 surface resistances at two cropland sites, *Journal of Geophysical Research: Atmospheres*, 122, 784–
914 801, <https://doi.org/10.1002/2016JD025975>, 2017.
- 915 Tapiador, F. J., Turk, F. J., Petersen, W., Hou, A. Y., García-Ortega, E., Machado, L. A. T., Angelis,
916 C. F., Salio, P., Kidd, C., Huffman, G. J., and de Castro, M.: Global precipitation measurement:
917 Methods, datasets and applications, *Atmospheric Research*, 104–105, 70–97,
918 <https://doi.org/10.1016/j.atmosres.2011.10.021>, 2012.
- 919 Taylor, K. E.: Summarizing multiple aspects of model performance in a single diagram, *Journal of*
920 *Geophysical Research: Atmospheres*, 106, 7183–7192, <https://doi.org/10.1029/2000JD900719>,
921 2001.
- 922 Udo; Becker, Andreas; Finger, Peter; Meyer-Christoffer, Anja; Rudolf, Bruno; Ziese, Markus: GPCP
923 Full Data Reanalysis Version 6.0 at 2.5°: Monthly Land-Surface Precipitation from Rain-Gauges
924 built on GTS-based and Historic Data., [https://doi.org/DOI: 10.5676/DWD_GPCP/FD_M_V7_250](https://doi.org/DOI:10.5676/DWD_GPCP/FD_M_V7_250),
925 2011.



- 926 Vermote, E: MOD09CMG MODIS/Terra Surface Reflectance Daily L3 Global 0.05Deg CMG V006
927 [data set], <https://doi.org/10.5067/MODIS/MOD09CMG.006>, 2015.
- 928 Wan, Z., Hook, S., Hulley, G: MOD11C1 MODIS/Terra Land Surface Temperature/Emissivity Daily
929 L3 Global 0.05Deg CMG V006 [data set], <https://doi.org/10.5067/MODIS/MOD11C1.006>, 2015.
- 930 Wang, K. and Dickinson, R. E.: Global atmospheric downward longwave radiation at the surface
931 from ground-based observations, satellite retrievals, and reanalyses, *Reviews of Geophysics*, 51,
932 150–185, <https://doi.org/10.1002/rog.20009>, 2013.
- 933 Wang, K., Ma, Q., Wang, X., and Wild, M.: Urban impacts on mean and trend of surface incident
934 solar radiation, *Geophysical Research Letters*, 41, 4664–4668,
935 <https://doi.org/10.1002/2014GL060201>, 2014.
- 936 Wang, Y., Zhao, X., Mamtimin, A., Sayit, H., Abulizi, S., Maturdi, A., Yang, F., Huo, W., Zhou, C.,
937 Yang, X., and Liu, X.: Evaluation of Reanalysis Datasets for Solar Radiation with In Situ
938 Observations at a Location over the Gobi Region of Xinjiang, China, *Remote Sensing*, 13, 4191,
939 <https://doi.org/10.3390/rs13214191>, 2021.
- 940 White, M. A., Thornton, P. E., Running, S. W., and Nemani, R. R.: Parameterization and Sensitivity
941 Analysis of the BIOME–BGC Terrestrial Ecosystem Model: Net Primary Production Controls, *Earth
942 Interactions*, 4, 1–85, [https://doi.org/10.1175/1087-3562\(2000\)004<0003:PASAOT>2.0.CO;2](https://doi.org/10.1175/1087-3562(2000)004<0003:PASAOT>2.0.CO;2),
943 2000.
- 944 Yang, D., Chen, H., and Lei, H.: Analysis of the Diurnal Pattern of Evaporative Fraction and Its
945 Controlling Factors over Croplands in the Northern China, *Journal of Integrative Agriculture*, 12,
946 1316–1329, [https://doi.org/10.1016/S2095-3119\(13\)60540-7](https://doi.org/10.1016/S2095-3119(13)60540-7), 2013.
- 947 Yang, R. and Friedl, M. A.: Modeling the effects of three-dimensional vegetation structure on surface
948 radiation and energy balance in boreal forests, *Journal of Geophysical Research: Atmospheres*, 108,
949 <https://doi.org/10.1029/2002JD003109>, 2003.
- 950 Zhang, C., Long, D., Zhang, Y., Anderson, M. C., Kustas, W. P., and Yang, Y.: A decadal (2008–
951 2017) daily evapotranspiration data set of 1 km spatial resolution and spatial completeness across
952 the North China Plain using TSEB and data fusion, *Remote Sensing of Environment*, 262, 112519,
953 <https://doi.org/10.1016/j.rse.2021.112519>, 2021.
- 954 Zhang, K., Kimball, J. S., Mu, Q., Jones, L. A., Goetz, S. J., and Running, S. W.: Satellite based
955 analysis of northern ET trends and associated changes in the regional water balance from 1983 to
956 2005, *Journal of Hydrology*, 379, 92–110, <https://doi.org/10.1016/j.jhydrol.2009.09.047>, 2009.
- 957 Zhang, K., Kimball, J. S., Nemani, R. R., and Running, S. W.: A continuous satellite-derived global
958 record of land surface evapotranspiration from 1983 to 2006, *Water Resources Research*, 46,
959 <https://doi.org/10.1029/2009WR008800>, 2010.
- 960 Zhang, K., Kimball, J. S., Nemani, R. R., Running, S. W., Hong, Y., Gourley, J. J., and Yu, Z.:
961 Vegetation Greening and Climate Change Promote Multidecadal Rises of Global Land
962 Evapotranspiration, *Sci Rep*, 5, 15956, <https://doi.org/10.1038/srep15956>, 2015.
- 963 Zhang, L., Yu, X., Zhou, T., Zhang, W., Hu, S., and Clark, R.: Understanding and Attribution of
964 Extreme Heat and Drought Events in 2022: Current Situation and Future Challenges, *Adv. Atmos.
965 Sci.*, 40, 1941–1951, <https://doi.org/10.1007/s00376-023-3171-x>, 2023.
- 966 Zhang, X., Huang, A., Dai, Y., Li, W., Gu, C., Yuan, H., Wei, N., Zhang, Y., Qiu, B., and Cai, S.:
967 Influences of 3D Sub-Grid Terrain Radiative Effect on the Performance of CoLM Over Heihe River
968 Basin, Tibetan Plateau, *Journal of Advances in Modeling Earth Systems*, 14, e2021MS002654,
969 <https://doi.org/10.1029/2021MS002654>, 2022.



970 Zhang, Y.: PML_V2 global evapotranspiration and gross primary production (2002.07-2019.08),
971 National Tibetan Plateau / Third Pole Environment Data Center, [data set],
972 <https://doi.org/10.11888/Geogra.tpdc.270251>, 2022.

973 Zhang, Y., Kong, D., Gan, R., Chiew, F. H. S., McVicar, T. R., Zhang, Q., and Yang, Y.: Coupled
974 estimation of 500 m and 8-day resolution global evapotranspiration and gross primary production in
975 2002–2017, *Remote Sensing of Environment*, 222, 165–182,
976 <https://doi.org/10.1016/j.rse.2018.12.031>, 2019.

977